SPECTROSCOPY OF QUANTUM EMITTERS AND THEIR APPLICATIONS

A Dissertation

by

XIAOHAN LIU

Submitted to the Graduate and Professional School of
Texas A&M University
in partial fulfillment of the requirements for the degree of

DOCTOR OF PHILOSOPHY

Chair of Committee,	Alexey Akimov
Committee Members,	Olga Kocharovskaya
	Philip Hemmer
	Dong Hee Son
Head of Department,	Grigory Rogachev

December 2021

Major Subject: Physics

ABSTRACT

Temperature sensing is crucial in many areas such as in biology research. Group IV color centers in diamond have many advantages over other sensors. Detailed research on Tin-vacancy (SnV) color center as thermometry is presented in this work, and a fiber thermometry probe based on Germanium-vacancy (GeV) is also demonstrated. Those results have shown the promising future of diamond color center thermometry and possibilities to combine multi color centers for more complicated thermal imaging.

Lead halide perovskite nanocrystal is a novel semiconductor that has gain much attention due to its extraordinary optical properties. Some of dark exciton properties such as its relative order to bright exciton in this nanocrystal still remain unclear mainly due to lack of dark exciton photoluminescence (PL). An intense dark exciton emission is demonstrated in this work taking advantage of strong quantum confinement. A systematic study on size dependency of dark exciton in this work also reveal the importance of quantum confinement in determining dark exciton properties and its future applications.

ACKNOWLEDGEMENTS

I would like to thank my advisor, Dr. Akimov, who has been very understanding and supportive through my whole PhD program. He maintain an open and free academic environment for whole team. His patience and enthusiasm encourage me through ups and downs of my PhD. I appreciate his guidance during every discussion, his patient explanation on every issue, from tedious setup debug to challenging theoretical analyses. I know I can always talk directly with him and obtained a brilliant inspiration.

I'm also grateful to my committee. Dr. Olga Kocharovskaya, she give us a lot of theoretical insight onto EIT and color centers. Dr. Philip Hemmer, he support us with essential equipment and expertise, from where our lab start to ramp up quickly. Collaboration with Dr. Don Hee Song's group enable the work in last part of this thesis. His imagination and professional advice harvest our research.

I am lucky to have spent two years with Ivan Cojocaru. As a senior student, he teach me how to build confocal microscope, run automate experiment with LabVIEW. I can't imagine how much support I get from this incredibly talented and hardworking colleague. His unmatched kindness and selflessness help benefit every member in lab even after his graduation.

Thanks to the collaboration with Mohit, we could manage to build the magnet cryostat and proceed with dark exciton research. I still remember those days when we work together till midnight. I'm so fortunate to interact with Dr. Vladimir Khmelenko and Sergei. Without their valuable advice in low temperature technologies, difficulties will

exponentially accumulate. I also thank Abdurrahman, he and Mohit do pioneer work in clean room for our lab one after the other. I'm grateful for collaboration with Sean Blakley, Zehua Han. Their support broaden my capability with experiments.

I extremely enjoy our collaboration with chemistry colleagues. Daniel Rossi bring us the idea of dark exciton within quantum confined palate. During his visit in physics department, we built setup almost from nothing and made so many things happened. I am thankful to three years' collaboration with Tian Qiao. Her excellent synthesize skill is the key for our perovskite nanocrystal research. Her enthusiasm in research continues to bring us new ideas about physics and chemistry.

One of the highlights for my PhD is my friends. They make college station a warmer place. Yanli Shi, Ankang Liu, Zhe He, the fruitful discussion with them deepen my understanding both in science and life. Thanks Zheng Lei, my defense celebration will be bleak without his excellent cooking.

All things will never be possible without the support of my mom. She give me a bright childhood even when darkness shrouded the life. Her sacrifices and unconditional love is the reason I could reach this point.

CONTRIBUTORS AND FUNDING SOURCES

Contributors

This work was supervised by a dissertation committee consisting of Professor Alexey Akimov [advisor] and Olga Kocharovskaya of the Department of Physics & Astronomy, Professor Dong Hee Son of the Department of Chemistry, and Professor Philip Hemmer of the Department of Electrical & Computer Engineering.

The data analyzed in Figure 3.1, Figure 3.2, Figure 3.5, Figure 3.6, Figure 4.2, were provided by Daniel Rossi, student of Professor Dong Hee Son. He also conduct in part of the data analyzed in Figure 3.4, Figure 3.8, Figure 4.4. The analysis for Figure 3.9 were provided by Professor Dong Hee Son. The data analyzed in Figure 2.3, Figure 2.4 were conducted in part by Masfer Alkahtani, student of Professor Philips Hemmer. The data and analyses depicted in Figure 2.7, Figure 2.8 were conducted in part by Sean Blakley of the Department of Physics. All other work conducted for the thesis (or) dissertation was completed by the student independently.

Funding Sources

Graduate study was supported by a fellowship from Texas A&M University. This work was also made possible in part by National Science Foundation (NSF, grants # 1836538, # 2003961) and Texas A&M T3, X-grant and College of Science Strategic Transformative Research Programs. Its contents are solely the responsibility of the authors and do not necessarily represent the official views of the NSF or Texas A&M University.

TABLE OF CONTENTS

Page

LIST OF FIGURES

Page

LIST OF TABLES

Page

CHAPTER 1

INTRODUCTION

1.1 All Optical Thermometry with Diamond Color Center

Color centers are defects in diamond. Their electrical state are highly localized, so we can treat their as atom like emitters. They gain lot of attention due to their extraordinary performance in applications such as quantum sensing[1], network[2], and memory[3]. Nitrogen vacancy is the first discovered and well-known color center, its long coherence time even at room temperature[4] could be extremely beneficial for quantum applications. NV can also be used to practical applications like magnetic field[5] and temperature sensing[1]. But some drawbacks of NV limit its further application, e.g. its large spectral diffusion. This is an effect mainly from local electric charge fluctuation[6], the spectrum of NV will drift with time and thus broaden the linewidth. Also the necessary microwave when using NV can generate extra heat and disturb accurate temperature sensing.

To solve those limitations, group IV color centers have gained more and more attentions due to their excellent optical and spin properties. As shown in Figure 1.1(a), the group IV color centers are formed by one atom and two adjacent vacancies along $\langle 111 \rangle$ direction of diamond. SiV is the first discovered and most well researched one among this group.[7] Other color centers like GeV, SnV and PbV, due to their similar crystal structure, have energy structure similar to that of SiV. Because of its inversion symmetry as shown in the Figure 1.1(a), this group of color centers are resilient to local electronic fluctuation in the first order[8]. Electric field fluctuation is considered to be the main reason for spectrum diffusion of NV, where dc stark shift will dynamically shift the energy level.[6] The

inversion symmetry in group IV color center, make orbital dipole momentum vanish.[8] Thus let those color centers free of perturbation from surrounding electric field. This property is extremely beneficial when implementing color centers in photonics platform and achieve solid state quantum devices.[8,9]

The energy level of this group of color centers is shown in Figure 1.1(b), ^2E_u excited state and ^2E_g ground state both have double orbital degeneracy. This degeneracy will then be lift by spin orbital coupling. Jahn-Teller interaction, a term refer to electron-phonon interaction, will shift the energy level of those orbital states and thus can also change the splitting effectively. The generated four states are all spin-1/2 degenerated, which can be further lifted by external magnetic field. The main disadvantage of this group of color center is their short coherence time. For example it is reported by Trusheim et al[10] that they only reach $T_2^* = 59 \pm 8\, ns$ at 5 K for SnV. There are also a lot of research trying to solve this issue by further cooling down to mK[11] or strain control.[9] The ground state splitting is becoming larger for SiV, GeV and SnV, namely 50GHz, 170 GHz and 850 GHz respectively,[7] due to larger atom. The larger ground splitting, the less phonon transition between states, and thus larger coherence time. In the research work done by Sohn, Meesala et al, they use strain to control the splitting and effectively improve the coherence time.[9]

Compared to NV, who emit 4% emission into ZPL, this group of color centers emit about 70% energy into ZPL.[12] With absent of magnetic field, transitions among stats, indicated by ABCD in Figure 1.1(b), are only among orbital degree of freedom and are spin conserving. In addition to that, Jahn-Teller interaction will shift energy level in color

centers and thus give us temperature dependent spectrum. Although over large temperature range, the spectrum position and linewidth will have T^3 behavior, within the small range of for normal biology application, e.g. 290k-320k, the temperature change of spectrum can be described by linear function with good accuracy. Temperature is a key factor in living organisms, e.g., cell division, enzyme reaction. Group IV color centers' large emission into ZPL, all optical temperature dependent transitions, combined together give us the opportunity to achieve all optical thermometry with color center, and take the advantage of diamond in biology sensing.

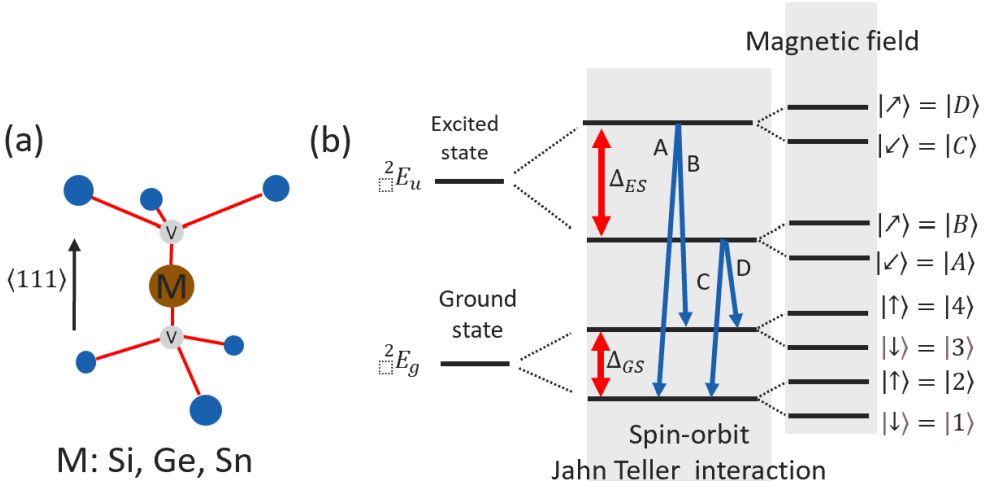

Figure 1.1 (a) Crystal structure of group IV color center. They consist of an implemented atom and two adjacent vacancies. The overall structure have inverse symmetry. (b) energy level of group IV color center

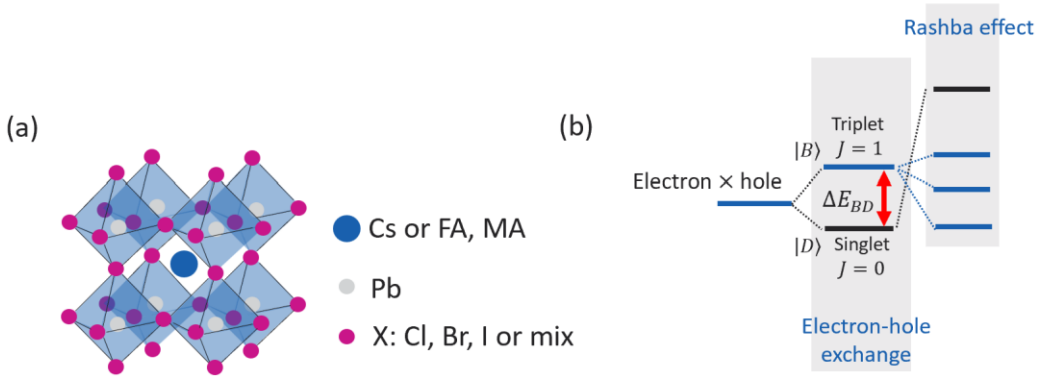

Figure 1.2 (a) Crystal structure of lead halide nanocrystal, there are two main types, fully inorganic (e.g. $CsPbX_3$) and inorganic-organic hybrid (e.g. $FAPbBr_3$). (b) Energy level of cesium lead halide nanocrystal

1.2 Dark Exciton in Strong Quantum Confined Lead Halide Perovskite Nanocrystal

Lead halide semiconductor with perovskite crystal structure (LHP) shown in Figure 1.2(a) is a novel material obtained more and more focus in recent year's research. Its capability have been shown in varies applications such as lasing[13], light emitting diode[14] and sola cell[15] due to its outstanding optical properties. Depend on its ingredient, there are mainly two types of this nanocrystal, fully inorganic and hybrid organic-inorganic. $MAPbX_3$ and $FAPbX_3$ are two examples of hybrid lead halide nanocrystals, where MA and FA are methyl ammonium and formamidimium respectively. $CsPbX_3$ is an example of fully inorganic LHP, which is also the one we focus on in our projects. Figure 1.2(b) shows the level structure of $CsPbX_3$.[16] Formed by electron and hole, the exciton has energy level with four degeneracies. Exciton fine structure will be generated when this degeneracy is lifted by electron-hole exchange interaction, an interaction between spin of electron and hole described by a Hamiltonian dominated by $\sigma^e \cdot \sigma^h$ term. This fine structure has two states, one is singlet and the other is triplet. The triple have totally angular moment $J = 1$.

It's optical active with nano second lifetime. The singlet have total angular momentum $J = 0$ and thus its transition is dipole forbidden. So this singlet state with microsecond lifetime is called dark exciton. One important property of dark exciton in $CsPbX_3$ is its magentic field dependency. The mix between bright and dark exciton can give dark exciton addtional oscillation strength and thus shorter lifetime.[17,18] The detail of this mixing process is decribed in Appendix C. The shorten of dark exiton lifetime under magnetic field, along with its long lifetime such as microsecond, are two fundamental sigatures that can help us identify the dark exciton in this type of nanocrystal.

When there is Rashba effect suggested by Becker, Vaxenburg et al, the order of this dark and bright exciton fine structure could be reverted[16] and make this $CsPbX_3$ the first semicondcutor with optical active ground state. But there is still debate on the lowest eergy level. In research work of Becker, Vaxenburg et al, they demenstrate their lifetime experimental data where no long compoment have been found, indicating bright exciton ground state in their analyse.[16] But in a research work with FAPbBr3, Tamarat, Bodnarchuk et al find that although there is no long component even at cryogenic temperature, a signlet ground state start to appear under high magneitc field up to 7T.[17] This means the ground state of this lead halide nanocrystal is acturally dark exciton. Our research is also trying to address this debate. We find strong quantum confinement is a key factor for access to dark exciton, and for futher study of its properties.

Quantum confinement refer to an effect when the nanocrystal size is smaller than exciton diameter, which is decribe by Bohr diameter, the electric state will change with nanocrystaal size. Quantum confinement is directly related to electron hole exchange

interrction, which result in dark bright exciton splitting.[16] It has been shown in previous study in CdSe QDs, that smaller size of QDs gives larger brigth dark splitting.[19] Strong quantum confinement enlarge bright dark splitting and coud give us facile access to dark exciton. Our research work was conducted with $CsPbX_3$ with strong quantum confinement. We demonstrated intense dark exciton emission and the important role of strong quantum confinement behind it.

1.3 Thesis Outline

Chapter 2 describes the experiment we have done on SnV and GeV in thermometry application. In section 2.2, the result demonstrate the capability of SnV as a quantum thermometry and we compare SnV's properties relative to SiV and SnV. In section 2.3, we combine GeV with fiber optics, to get better sensitivity and good spatial resolution.

Chapter 3 describe our research work on dark exciton of $CsPbX_3$ nanocrystal. In section 3.2, we demonstrate the intense dark exciton emission as ground state from $CsPbBr_3$ utilizing strong quantum confinement. In section 3.3, we further explore the important effect of quantum confinement onto dark exciton properties in both $CsPbBr_3$ and $CsPbI_3$.

CHAPTER 2

ALL OPTICAL THERMOMETRY BASED ON GEV AND SNV*

In this chapter, we report optical temperature measurements using the tin-vacancy (SnV) color center in diamond and show sensitivity better than 0.2 K in 10 s integration time. Also, we compare the relative merits of SnV with respect to SiV and GeV for luminescent thermometry. These results illustrate that there are likely to be many future options for nanoscale thermometry using diamonds. Then we develop a highly accurate fiber-optic micro thermometer employing exclusively optical interrogation of germanium vacancy quantum emitters in diamond. This thermometer possesses a thermal resolution of approximately $20\ mK/\sqrt{Hz}$ and a spatial resolution of 25μm.

2.1 Introduction

2.1.1 Fluorescent Diamond in Temperature Sensing

Temperature is a key factor in living organisms, especially during critical cell division, gene expression, enzyme reaction, and metabolism stages.[20,21] Luminescent nano thermometry is a promising approach to monitor small, and highly local, variations of temperature within bio-systems. In recent years, intracellular temperature mapping has been reported using quantum dots (QDs),[22-25] organic dyes,[26-30] fluorescent polymers,[31]

*Parts of this chapter are reprinted with permission from, Alkahtani, M. *et al.* Tin-vacancy in diamonds for luminescent thermometry. *Applied Physics Letters* **112**, 241902, doi:10.1063/1.5037053 (2018). And adapted with permission from, Blakley, S. *et al.* Fiber-Optic Quantum Thermometry with Germanium-Vacancy Centers in Diamond. *ACS Photonics* **6**, 1690-1693, doi:10.1021/acsphotonics.9b00206 (2019). Copyright 2021 American Chemical Society. And adapted with permission from, Blakley, S. M. *et al.* Photonic-Crystal-Fiber Quantum Probes for High-Resolution Thermal Imaging. *Physical Review Applied* **13**, 044048, doi:10.1103/PhysRevApplied.13.044048 (2020). Copyright 2021 by the American Physical Society

and thermal imaging.[32] Most of these fluorescent nanothermometers are good imaging agents and sensitive enough to detect a sub-kelvin rise in temperature in living cells.[1,22-24,27,29,31-33] However, many of the existing nanothermometers are limited by photostability,[34] toxicity,[22-29,34,35] and chemical environmental sensitivity.[31] Furthermore, up conversion nanoparticles (UCNPs) have shown great potential for intracellular temperature sensing with 0.2–0.5 K[36-39] precision in living cells; however, they are limited by low quantum efficiency.[40]

To overcome the above-mentioned limitations, fluorescent diamonds were recently demonstrated to be capable of precise optical temperature sensing in living organisms.[1] Fluorescent diamonds have remarkable optical, chemical, and biocompatibility properties.[41-43]. Different types of diamond color centers can have fluorescence range between 500nm to 800nm,[7] could meet the requirement for different scenario. Its exceptional optical stability even at nano diamond level[44] broaden its application to micro scale chemistry or biology study. Due to its stable crystal structure, diamond is inactive to most of the chemicals. It has been shown that nano diamonds are not toxic to many kinds of cells. Cells can also grow on nano diamond coated substrates.[45] Diamond's high thermal conductivity also helps to make it relatively easy to catch up the thermal change of samples. Fluorescent diamond's optical stability, chemical resilience and biocompatibility make it a good probe to do thermal sensing in addition to commonly used quantum dots or organic dyes.

2.1.2 All Candidates of Color Centers for Thermometry

So far, the color center that promises the most accuracy is the nitrogen-vacancy (NV) which uses a magnetic spin transition whose resonance frequency is sensitive to thermally induced lattice expansion.[46,47] The NV color center has been reported to provide sensitivity down to $1.8\,mK/\sqrt{Hz}$ in a pure bulk-diamond crystal and $200\,mK/\sqrt{Hz}$ in nano diamonds having a spatial resolution of 200 nm in living cells.[1] However, measuring temperature with the NV spin transition requires excitation by microwave radiation which can perturb living organisms. This heating can be a possible source of confusion for accurate local temperature measurements. In addition, non-axial magnetic fields also cause a shift in the NV spin resonance that can mimic temperature effects.[48,49] Furthermore, living cells have been reported to produce an electric field, especially near their membranes[50] which can be detected by the NV center in diamonds,[51] resulting in a shift of the NV center spin resonance similar to temperature effects.

Recently, another approach, namely, utilization of temperature shifts of the zero-phonon line (ZPL=638 nm) of the NV center, has been reported to provide a sensitivity of $200\,mK/\sqrt{Hz}$ around room temperature and spatial resolution better than 100 nm.[52-55] However, the nano diamond to nano diamond uncertainty in the reported measurement exceeded 20 K, and there were significant variations in the slope of frequency shift vs temperature. Therefore, the method requires full calibration of each nano diamond used, even for the relative temperature measurement. Moreover, frequency shift measurements are complicated by the presence of other than temperature factors, such as local strain

surface defects, and other impurities affect the ZPL visibility of the NV center, which is often only barely visible at room temperature in nano diamonds.

To overcome these limitations, it is only necessary to note that other color centers, having much stronger ZPL optical transitions, also experience frequency shifts due to temperature changes. In particular, the silicon-vacancy (SiV) and germanium-vacancy (GeV) centers in diamonds have been reported to measure temperature using frequency shifts of their narrow ZPL optical transition. At room temperature, the SiV color center has shown temperature sensitivity down to $360\ mK/\sqrt{Hz}$ in bulk diamonds and $521\ mK/\sqrt{Hz}$ in 200 nm nano diamonds at room temperature.[55] Also, at room temperature, the GeV color center has demonstrated a temperature sensitivity of $300\ mK/\sqrt{Hz}$ in bulk diamonds.[56] Another alternative is the recently discovered tin-vacancy (SnV) color center in diamonds.[57] Like the SiV and GeV, the tin atom sits on an interstitial site between two neighboring half vacancies in the diamond crystal. It has been incorporated into diamonds via ion implantation and subsequent high-temperature annealing. The SnV center exhibits a sharp zero phonon line at 620 nm at room temperature. At cryogenic temperatures, this line splits into four peaks where it has an exceptionally large ground state splitting (850GHz at low temperatures), which makes it of special interest for picosecond-pulse quantum storage applications.

In section 2.2, we show that SnV is very sensitive to temperature (near room temperature) and is therefore a good candidate for luminescent thermometry in diamonds. We also compare the relative merits of SnV to SiV and GeV for temperature measurements. Their similar sensitivities suggests that many more examples will be discovered in the future.

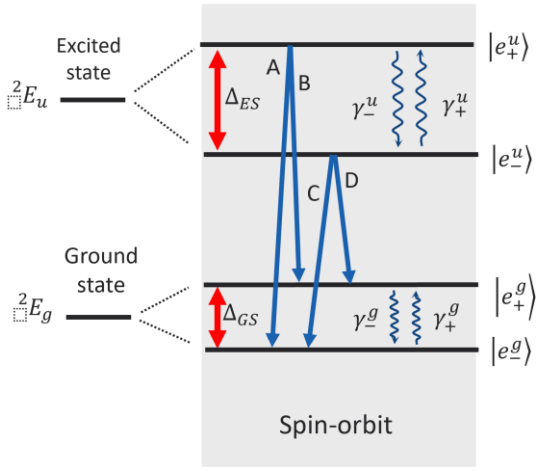

Figure 2.1 Illustration of phonon transition within group IV color centers

2.1.3 Mechanism in GeV and SnV for Sensing Temperature

The spectral shifts of the ZPLs for GeV, SiV or SnV are due to the phonon mixing to the electrical state.[56,58-65] A more detailed discussion has been done in previous work.[65] Here we will briefly introduce the main mechanism involved.

As shown in Figure 2.1, there are four transitions in SiV, GeV or SnV. Excited state and ground state split due to spin-orbital interaction. Electron-phonon interaction contributed to the temperature change of linewidth, state splitting and spectral line positions. By changing the phonon transition rate $\gamma_{(+,-)}^u$, decay rate of excited state will be modified, thus affect its linewidth. At lower temperature, single phonon transition is dominated, the linewidth is linear dependent on temperature. At higher temperature, two phonon processes will dominate, and linewidth will be dependent on temperature in T^3 manner.

Line position and splitting change share the same origin, that is the state energy shift due to electron-phonon interaction, i.e., δE_- and δE_+, where + and – correspond to upper and

lower branch of excited state or ground state. $\delta E_+ - \delta E_-$ is the line position shift, and $\delta E_+ + \delta E_-$ is the splitting, which have T^3 and T^2 dependence respectively.

Even though both line position and line width have T^3 behavior at high temperature, within small range above room temperature like 300 K to 315 K, we can still apply linear approximation. Besides, linewidth could also be approximate linear if $\hbar\Delta/k_B$ is large, which is exactly the case for SnV, $\hbar\Delta/k_B \sim 144\ K$. This approximate linear dependence on temperature make diamond color centers even more suitable for thermometry applications.

2.1.4 Diamond Thermometry based on Fiber Optics

Spatially resolved optical thermometry has facilitated many major innovations in important areas of research, greatly benefiting cell biology,[1,66] semiconductor development,[67] and cancer medicine.[68,69] Nanoparticle sensors[70,71] have gain a lot of attention due to their small sensor volume enabled high spatial resolution. With all advantages we introduce in previous subsection, micro and nanoscale diamond with silicon-, tin-, and germanium-vacancy (GeV) have demonstrated excellent potentials in achieving high spatial resolution and accurate vivo thermometry. Among these, GeV centers emit a high fraction of fluorescence into the zero-phonon line (ZPL),[63,72] thereby reducing heating due to conversion of pump light into phonons. However, the GeV center ZPL emission lies outside the biological transparency window,[73] harming the ability to collect signal with traditional microscopy solutions in an in vivo environment. This limitation could be overcome by using the fiber thermometry technology developed

previously, where optical fiber enable in situ excitation and signal collection. By combining GeV diamond and fiber platform, we can create a highly accurate, high spatial resolution, all-optical fiber GeV thermometer.

2.2 Tin-vacancy in Diamonds for Luminescent Thermometry

Given the advantage of fluorescent diamond over other emitters, we move forward to investigate the tin-vacancy (SnV) color center in diamonds, reveal its potentials in temperature sensing. In this section, we report optical temperature measurements using the tin-vacancy (SnV) and show sensitivity better than 0.2 K in 10 s integration time. Also, we compare the relative merits of SnV with respect to SiV and GeV for luminescent thermometry.

2.2.1 Experimental Setup

In this experiment, we used an ultrapure diamond crystal (100) (Element six) implanted with silicon, germanium, and tin elements with an implantation dose of 1012 ions/cm^2. To create vacancies around the implanted atoms, the implanted sample was annealed first to 800 ° and then to a much higher temperature (1500°) in a vacuum for several hours. For optical characterizations of the implanted color centers, we used a custom-built confocal laser scanning microscope equipped with a visible-near-infrared objective (NA=0.90), a single mode green laser (max power=150 mW), a custom-built spectrometer, and a Janis ST-500 cryostat unit as shown in Figure 2.2. The laser scans the sample in x-y directions using Thorlabs GVS 212 Galvano (10 mm mirrors) scanners. The collected optical

emission from the SnV was filtered with notch filters to remove light from the excitation laser and analyzed by the spectrometer and photon counter in the detection unit.

2.2.2 SnV Spectrum Analysis

The photoluminescence (PL) spectrum of the SnV revealed two strong peaks at 620 nm and 647 nm at room temperature as shown in Figure 2.2(b). Like SiV and GeV, these peaks shift with temperature due to the phonon mixing.[56,58-65] This is because the electron–phonon interaction is much faster than the spontaneous decay rate of the exited state over a wide range of temperatures, resulting in a strong temperature- dependence of both the line width of the transition and a shift of its spectral position.[56,65] In Figure 2.2(c), we demonstrate optical temperature sensing with the SnV color center. We observed that the zero-phone line (ZPL) peak of the SnV (620 nm) shifts to the red as the temperature increases. Although the SnV ZPL peak position changes non-linearly from low temperature (40 K) to room temperature (data will be shown later), it is approximately linear over a small temperature range (298 K–315 K) of interest for thermometry in biological systems. Fitting the experimental data shown in Figure 2.2(c) to a linear equation gives a slope of $\Delta\lambda/\Delta T = 0.0142 nm/\ ^{\circ}K$ as shown in Figure 2.2(d), which provides the calibration for temperature measurements. Similarly, temperature measurements were also carried out for the other peak (647 nm) in the SnV emission spectrum. The susceptibility was similar, but since this peak is weaker, it demonstrates lower sensitivity for temperature dependence. So, this peak will not be discussed in this

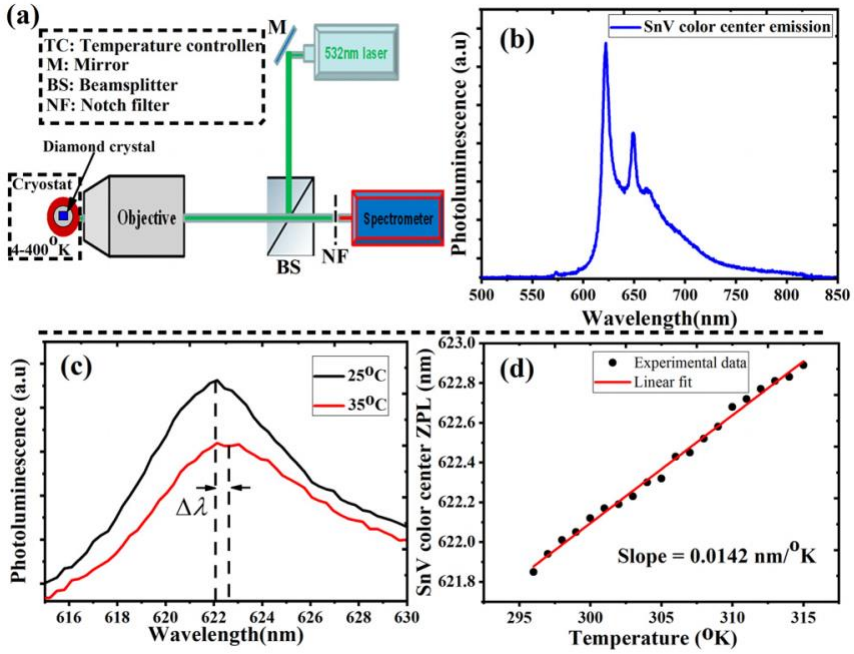

Figure 2.2* (a) An optical setup for optical temperature measurements consists of an excitation green laser, a custom-built spectrometer, and a cryostat unit. (b) Typical photoluminescence spectrum of the tin-vacancy (SnV) color center in diamond. (c) Photoluminescence emission spectra of the SnV color center in diamond under 532 nm illumination as a function of different temperatures; (25° black) and (35° red). (d) Linear fitting of the zero-phonon line (ZPL) of the SnV color center change as a function of ambient temperature.

study. It is also important to perform optical temperature measurements on the SnV color center over a wide range of temperatures from low to high (50 K–400 K) to see how well it follows the predicted T^3 temperature-dependence. Figure 2.3(a) shows that a linear dependence of the SnV ZPL peak position shift as a function of temperature persists over a relatively large range (280 K–400 K) with the slope equal to 0.0141 nm/K. This result agrees with the slope measured above for the SnV over a smaller range of temperature

* Reprinted from Alkahtani, Cojocaru et al. 2018

changes. Over a much wider range of temperatures (50 K–400 K), Figure 2.3(b) demonstrates a T^3 temperature dependence of the SnV ZPL position which agrees with

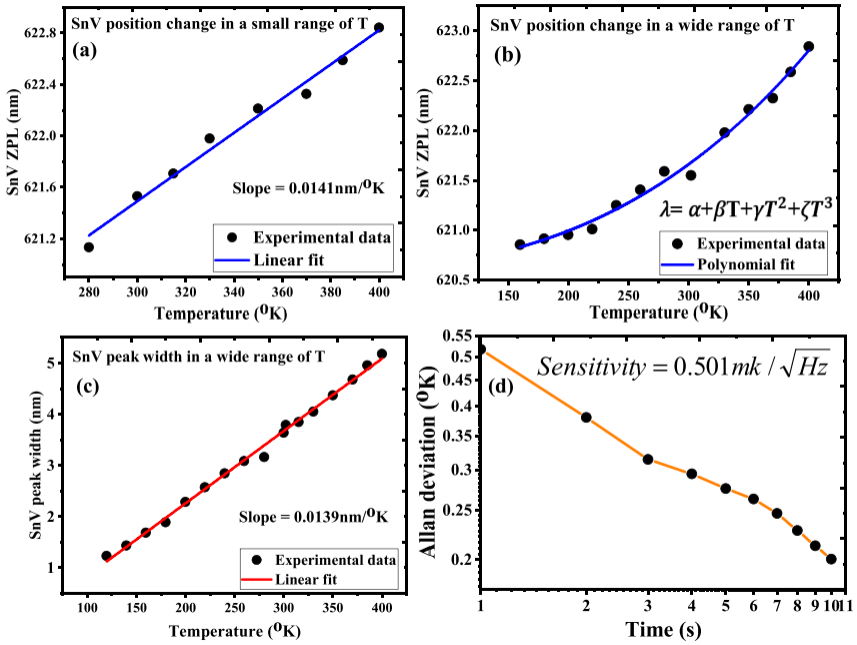

Figure 2.3* (a) A linear fitting of the SnV zero-phonon line (ZPL) position change as a function of temperature changes over a relatively wide range (280K–400 K). (b) Non-linear fitting of the SnV zero-phonon line (ZPL) position change as a function of low-high temperature changes over a wide range (170K–400 K). (c) A linear fitting of the SnV zero-phonon line (ZPL) width change as a function of temperature changes over a wide range (120K–400 K). (d) Allan deviation plotting for the ZPL peak position changes at room temperature over integration time. The slope indicates a square-root dependence of temperature measurement resolution. Temperature sensitivity in this experiment is $500\ mK/\sqrt{Hz}$

SiV and GeV color centers over the same temperature range as reported in previous studies.[56,65] Here, we note that the ZPL width also depends on temperature. Therefore, we also studied the feasibility of using the SnV center ZPL width vs temperature as another thermometry signal, as shown in Figure 2.3 (c). Fitting the experimental data to a linear

* Reprinted from Alkahtani, Cojocaru et al. 2018

equation gives a slope of 0.0139 nm/K. As seen, unlike the frequency shift, the linear dependence of the ZPL width vs temperature remains linear over a very wide range of temperatures (120 K–400 K).

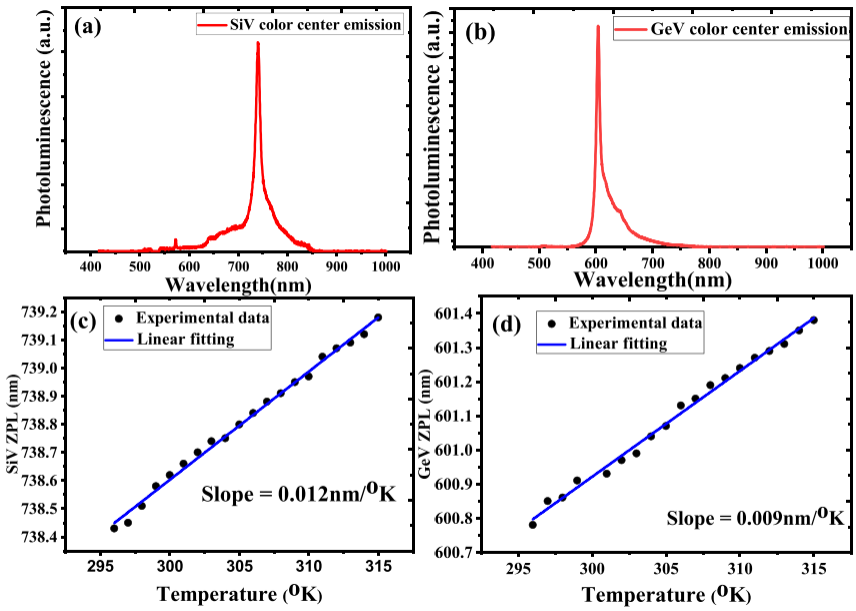

Figure 2.4* (a and b) Photoluminescence emission spectra of the SiV and GeV color center in diamond under 532 nm illumination peaked at 738 nm and 602 nm, respectively. (c and d) Linear fitting of the zero-phonon lines (ZPL) of the SiV and GeV color centers changes as a function of ambient temperature over a small range (298 K–315 K)

This provides an independent calibration for temperature measurements using the SnV color center in diamonds. Note that the dependence of the ZPL linewidth on the temperature is discussed in detail in previous work.[65] Briefly, this occurs because, at intermediate temperatures (i.e., when $T \sim \hbar\Delta/k_B$ but not yet $T \gg \hbar\Delta/k_B$), the single-phonon mixing is the dominant process. Of course, at higher temperatures, the T^3 dependence associated with the two-phonon process dominates for the linewidth, just as

* Reprinted from Alkahtani, Cojocaru et al. 2018

for the center-frequency shift. Since the SnV has an excited state splitting $\Delta \approx 3THz$ which is 3 times bigger than for the GeV center ($\Delta \approx 1THz$) and 12 times bigger than for SiV ($\Delta \approx 0.25THz$), the $\hbar\Delta/k_B$ factor is not as large for SnV. Specifically, $\hbar\Delta/k_B$ is 12 K for SiV, 47 K for GeV, and 144 K for SnV. Thus, room temperature is still not in the $T \gg \hbar\Delta/k_B$) limit. Therefore, a linear dependence of the SnV width vs temperature over a much broader range is quite reasonable for this color center.

2.2.3 Comparation between SnV and GeV, SiV

To compare the SnV color center with previously studied SiV and GeV color centers, we performed similar optical temperature measurements using SiV and GeV implanted in the same diamond crystal over the same temperature range. As in previous studies, the SiV and GeV color centers show ZPL lines peaked at 738 nm and 602 nm as shown in Figure 2.4(a) and (b), respectively. Like SnV, both SiV and GeV color centers showed a red shift of their optical ZPLs as the diamond temperature increases as shown in Figure 2.4(c) and (d). Fitting the experimental data to a line showed slopes equal to $\Delta\lambda/\Delta T = 0.012nm/\ ^{\circ}K$ and $\Delta\lambda/\Delta T = 0.009nm/\ ^{\circ}K$ for SiV and GeV color centers, respectively. These results are in good agreement with those previously reported in Refs.[55,56]. Table 2-1 compares optical temperature measurements using SnV, SiV, and GeV color centers in the temperature range of biological applications. As seen, SnV shows a slightly higher temperature susceptibility but similar sensitivity. To explain the higher susceptibility $\Delta\lambda/\Delta T$ of the SnV compared to SiV and GeV color centers, we note that the line center shift of the ZPL line normally has a universal T^3 behavior as long as the line is not split

into components and Boltzmann distribution does not strongly affect the relative level population.[65] This is because it depends on the spin phonon coupling strength χ which varies from color center to color center and in principle needs to be calculated in each case. Naively, one can argue that the external shells of a bigger atom should be stronger

Table 2-1* A summary of temperature susceptibility ($\Delta\lambda/\Delta$T) and thermometer sensitivity measurements over a small range of temperature changes (298 K–315 K) using SnV, SiV, and GeV color centers in diamond

Color Center in diamond	Temperature susceptibility $(\Delta\lambda/\Delta T)$	Sensitivity for 10s	Temperature range
Tin-vacancy (SnV)	0.0141nm/K (11GHz/K) this work	0.142mK this work	298 K-315 K
Silicon-vacancy (SiV)	0.012nm/K (6.8GHz/K) agrees with Ref[55]	0.134mK this work	298 K-315 K
Germanium-vacancy (GeV)	0.009 nm/K (6.8 GHz/K) agrees with Ref[56]	0.156mK this work	298 K-315 K

coupled with phonons in the matrix. Nevertheless, for Germanium and Silicon vacancies, the spectral shift of the lines is nearly the same if calculated in frequencies, while for SnV, it is almost a factor of two stronger, clearly indicating that size is not the only factor. Full understanding of this fact requires careful quantum mechanical calculations which are beyond the scope of this study.

* Reprinted from Alkahtani, Cojocaru et al. 2018

Finally, since the minimum detectable temperature fluctuations are governed by the integration time and fluorescence intensity, it is important to estimate SnV temperature sensitivity vs measurement time. So, we measured the Allan deviation of the temperature sensitivity using the ZPL peak position near room temperature up to 10 s of integration time as shown in Figure 2.3(d). This deviation plot shows a square root dependence (indicative of shot noise) giving a minimal detected temperature change of $500\ mK/\sqrt{Hz}$. This means that the SnV color center can be used for temperature measurements with resolution better than 0.2 K in 10 s integration time for a wide range of temperatures.

While the optical signal level was kept nearly the same for all color centers, their number/collection efficiency was smaller (leading to a signal of 4×10^6 counts instead of 7×10^6 counts in Ref.[56] than that in previous work, thus providing a bit less sensitivity (see Table 2-1). Nevertheless, it may be expected that due to the larger slope, SnV should have larger sensitivity. This advantage is nevertheless compensated by the fact that only about 20% of the SnV emission is concentrated in the ZPL compared to around 60%–70% for other color centers. Thus, the useful signal is a factor of 3–4 lower and shot noise limited performance is therefore a bit less than a factor of two worse. This loss is very close to the win in susceptibility, thus keeping the sensitivity at the level of other color centers. But a higher temperature annealing could increase the fraction of ZPL in the spectrum up to 80%,[57] which should allow realization of full, potentially twice better sensitivity of the SnV center

2.3 Fiber Optics Germanium-vacancy thermometry

In this section, we develop a highly accurate all optical thermometer with germanium vacancy in diamond. This thermometer possesses a thermal resolution of approximately 20 $mK/\sqrt{Hz}$ and a spatial resolution of 25μm.

2.3.1 Experimental setup

An approximately 2 mm by 2 mm by 1 mm single-crystal bulk diamond sample was irradiated at two locations (Figure 2.8 inset, a and b) with 80 keV Ge particles at a dose of between $10^{14}/cm^2$ and $10^{15}/cm^2$ and then annealed at 1500 °C, forming distinct 100 μm diameter implantation regions, with region b possessing the highest GeV concentration. Region b was optically interrogated by positioning the cleaved end of a 50 μm core-diameter commercial optical fiber against it and coupling laser light from the 532 nm second harmonic of a diode-pumped Nd: YAG source into the opposite end of the fiber (Figure 2.8). The sample was attached with a thermal adhesive to a copper heat-sink connected to a closed loop temperature controller capable of providing 1 mK accuracy between 20 and 50 °C. The combined temperature controller assembly was mounted to a 3-axis linear translation stage for accurate positioning of the sample in front of the fiber. The GeV signal was collected by the fiber and separated from the 532 nm pump by a notch filter before being imaged onto a 0.01 nm resolution narrow band spectrometer.

The sample temperature was varied linearly between 20 and 50 °C in 0.5 °C steps, and multiple GeV fluorescence spectra were collected by the spectrometer for each

temperature increment. The number of fluorescence spectra per temperature step was determined by the step dwell time and the 500 ms exposure time of the camera.

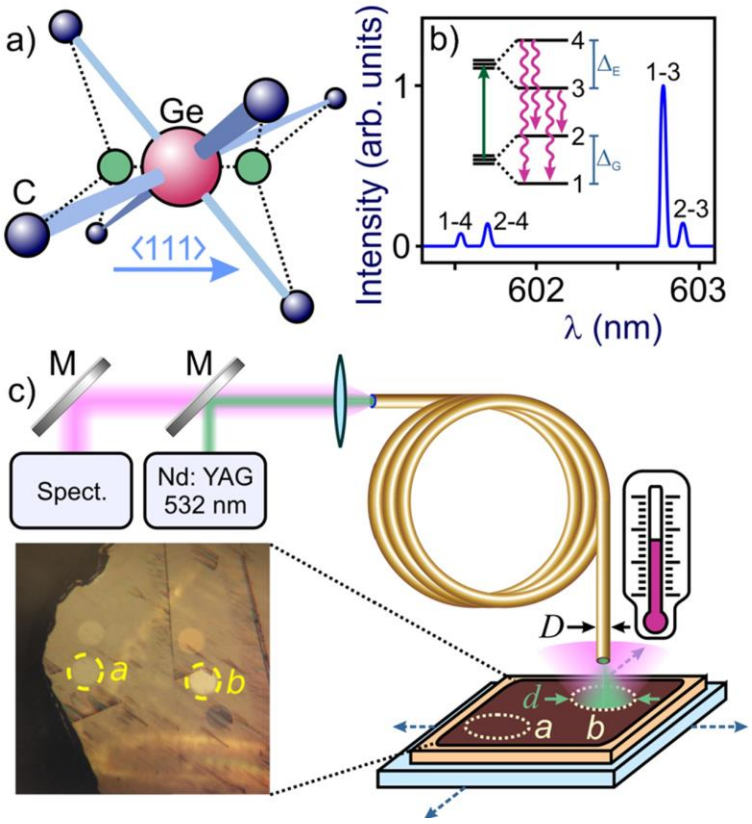

Figure 2.5* (a) Carbon (C) lattice structure of GeV defect in diamond along the ⟨111⟩ axis. A germanium atom (Ge) lies between two lattice vacancies (V). (b) Level structure (inset) and PL spectrum of GeV center. Four optical transitions (wavy red arrows, inset) account for ZPL peaks in the PL spectrum; (b) Level structure (inset) and PL spectrum of GeV center. Four optical transitions (wavy red arrows, inset) account for ZPL peaks in the PL spectrum; the peak of interest occurs around 602 nm. (c) Diagram of the GeV fiber thermometer experiment. Laser light is coupled to different 100 diameter GeV implantation regions via a 50 μm core-diameter optical fiber; GeV fluorescence is collected by the fiber and coupled into a spectrometer through a 532 nm notch filter. Implantation regions are interrogated individually by translating the sample with a 3-axis translation stage. Temperature controller adjusts diamond temperature

* Reprinted from Blakley, Liu et al. 2019

2.3.2 GeV spectrum fitting and signal to noise ratio

The GeV center in diamond is formed when two adjacent diamond lattice carbons are replaced with lattice vacancies and an interstitial germanium atom (Figure 2.5 (a)), forming a split vacancy color center.[65] An electron becomes trapped in one of these vacancies, creating spin 1/2 doublet ground and excited states possessing zero field energy splitting of approximately 180 GHz and 1.1 THz (Figure 2.5 (b) ΔG and ΔE), respectively.[64,72,73] In this experiment, we focus on the 1−3 transition (Figure 2.5 (b)) to implement temperature sensing. This transition possesses the highest photoluminescence (PL) amplitude, appearing as a single peak around 602 nm at room temperature.

Temperature-dependent changes in the PL signal were ascertained by fitting the fluorescence spectrum of the GeV ZPL and phonon sideband. Different Lorentzian functions are used depend on the PL signal-to-noise ratio for that measurement. In general, the most accurate fit to the spectral data was provided by a double Lorentzian function $L_2 = \lambda_w h/[\pi(\lambda - \lambda_c)^2/\lambda_w^2 + 1] + \lambda_{w2} h_2/[\pi(\lambda - \lambda_{c2})^2/\lambda_{w2}^2 + 1] + b$, (Figure 2.6 (a) and (b), orange traces), where λ, λ_c, λ_w, λ_{c2},λ_{w2} are the spectral wavelength, center wavelength and FWHM of the first and second Lorentzian fit peak respectively. The parameters h, h_2 and b correspond to the height of both Lorentzian fit peaks and the offset of the spectral baseline amplitude from zero respectively. A single Lorentzian function (L_1) provides a somewhat accurate fit for data taken at lower laser powers that remains stable for spectra taken across the entire temperature range (Figure 2.6 (a)). The double Lorentzian function sometimes (L_2) fails to accurately fit these noisier spectra, generating errors in the temperature accuracy and resolution calculations for these lower power

levels. However, for the higher laser power spectra, the L_2 fit is much more stable across the entire temperature range than the L_1 fit Figure 2.6, purple dashed traces), and provides a much more accurate fit, allowing for sensitive temperature measurements.

To determine what experimental parameters limit the spatial and temperature resolution of this measurement, the peak amplitudes for spectra taken with 500 ms exposure time (Figure 2.6(c)) were plotted versus laser power (Figure 2.6(d), blue trace). The peak amplitude and signal-to-noise ratio (SNR) were found to depend linearly on laser power

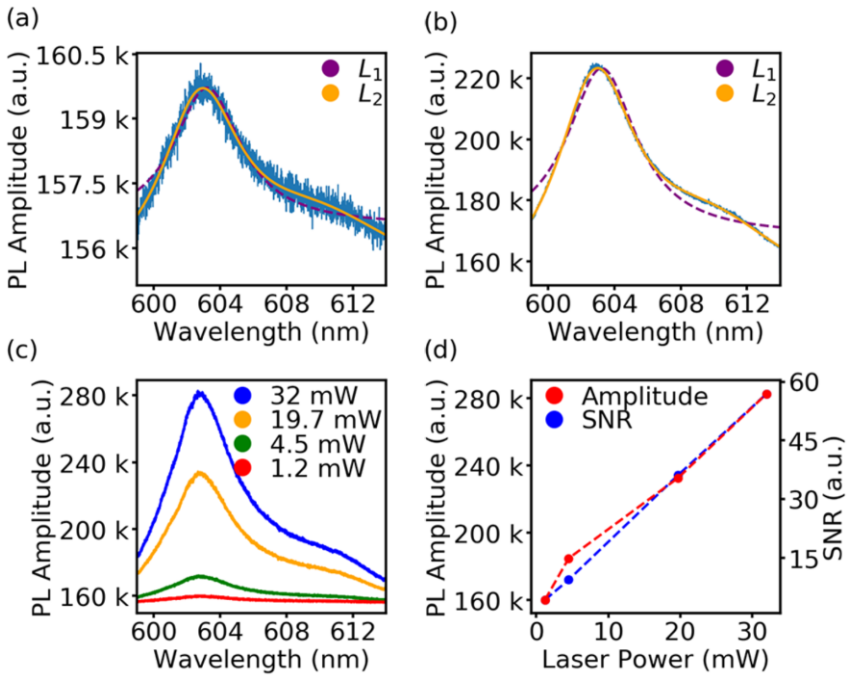

Figure 2.6* Single and double Lorentzian fit functions (purple, orange traces) for spectra collected with laser powers of (a) 1 mW and (b) 20 mW at 500 ms exposure time. (c) Fluorescence spectra collected at different laser powers. (d) Amplitudes of fluorescence peaks in (c) plotted versus laser power (red trace). SNR as a function of laser power (blue trace)

* Reprinted from Blakley, Liu et al. 2019

(Figure 2.6(d), blue and red traces respectively). The signal-to-noise ratio (SNR) was calculated by dividing the peak amplitude by the maximum noise amplitude at the top of the peak, which is a manifestation of both the detector dark current and laser amplitude fluctuations. This linear dependence of the SNR and peak amplitude on laser power determined that the GeV centers in region b were not being saturated by the incident laser light, as a nonlinear dependence of fluorescence amplitude on pump laser power would be expected in that situation. Therefore the fiber core diameter may be reduced until saturation occurs to enhance spatial resolution without affecting the collected signal or the SNR. Employing a higher numerical aperture (NA) fiber will enhance the fluorescence collection efficiency, permitting the use of lower laser powers while maintaining signal amplitude, thereby improving SNR by reducing detected thermal noise resulting from laser power fluctuations

2.3.2 Thermometry calibration and accuracy, resolution analysis

To produce a calibration curve, the exposure time was increased to 6 s and the temperature was incremented in 0.5 °C steps between 20 and 40 °C, with each step possessing a dwell time of 3 min. λ_w (Figure 2.7(a), dotted blue trace) and λ_c were extracted from the L_2 fit to the GeV spectra, and the average and standard deviation of both peak parameters for n data points were calculated for each temperature increment, where only data points collected once the temperature measured by the thermistor (Figure 2.7 (a), black circles) had stabilized to within 10 mK of the temperature set point (Figure 2.7 (a), dashed red trace) were used to calculate the average and standard deviation of the peak parameters.

The calibration curves for λ_w and λ_c (Figure 2.7(b) blue circles and black squares) possessed slopes of 0.013 and 0.008 nm/k for 8 averages per data point over 45 s per temperature step at a laser power of 30 mW. These slope values agree with measurements found in the literature.[56,74] Standard deviation error bars for data points in Figure 2.7 (b) were too small to be visible and thus were omitted from the plot.

In this experiment, the dependence of λ_c on temperature tends to be less linear than λ_w (Figure 2.7(b)), possessing a temperature-dependent change in the slope of λ_c over the whole temperature range (Figure 2.7(b), short, dashed lines). According to the literature,[56] λ_c and λ_w should be equally effective measures of temperature; however, λ_c measurements possessed 25% worse accuracy, attributed to this temperature dependent slope of λ_c. Additionally λ_c is more susceptible to mechanical vibrations and other environmental effects on the measurement apparatus, causing transient shifts in λ_c of nonthermal origin. λ_w measurements possess none of these drawbacks.

A more detailed description of accuracy and resolution for our thermometry is in Appendix A. Namely, the probe accuracy as a function of averaging time $\delta T_{acc} = \delta m_n \langle\langle \lambda_w \rangle_n \rangle_T$ was calculated by multiplying the slope error (δm_n) of the linear fit to temperature as a function of peak width (λ_w) by the n-sample average per temperature step (T_i) of λ_w averaged over the entire temperature range (T) (Figure 2.7(c)). δm_n was generated from a linear regression of n temperature measurements per T_i versus their n corresponding λ_w values. The temperature resolution of the probe defined as the thermal noise over a given bandwidth was calculated by plotting the Fourier transform of $m(\lambda_{w,i} - \langle \lambda_w \rangle_{T_i})$ as a function of noise frequency, where $\lambda_{w,i}$ are peak width measurements at T_i ,

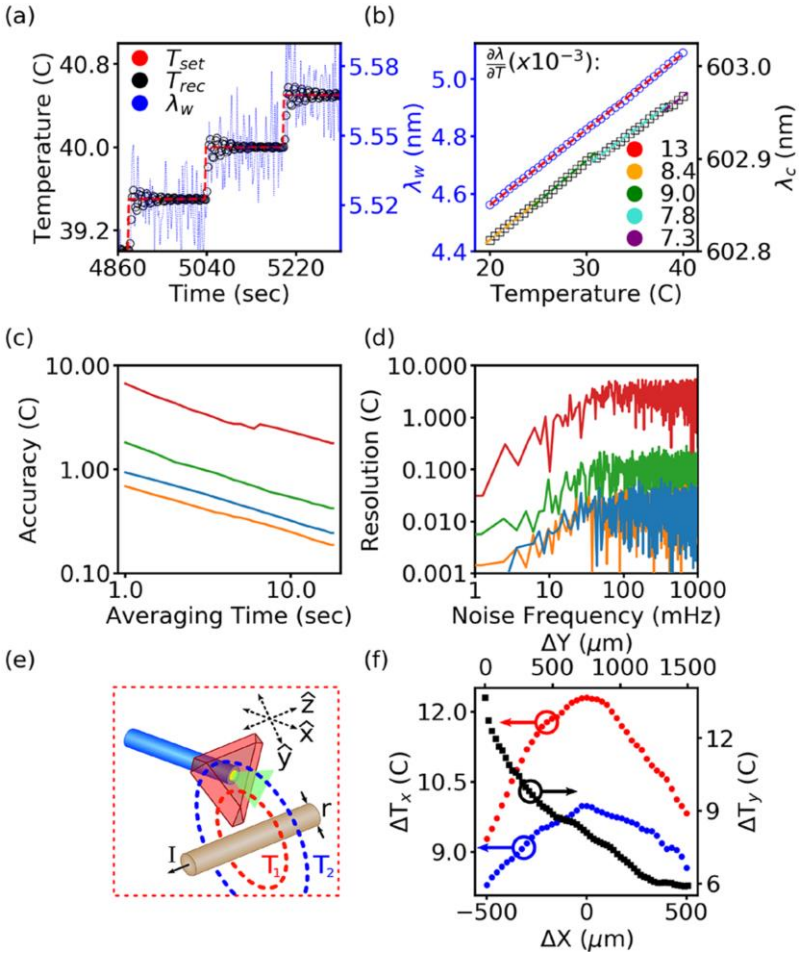

Figure 2.7* (a) Plot of measured temperature versus time for a step dwell time of 3 min. The thermal controller takes more than 2 min to fully settle (black points) to within 10 mK of the set temperature (dashed red trace). Peak width measurements (dotted blue trace) increase stepwise, following temperature steps. (b) Plot of GeV fluorescence peak width (λ_w, blue circles) and center wavelength (λ_c, black squares) versus temperature. Data points correspond to an average of 8 λ_w or λ_c measurements taken over 45 s. The linear fit to λ_w and λ_c versus temperature possesses slopes of 0.013 (dashed red trace) and 0.008 nm/K, respectively. Changes in slope of λ_c over small temperature ranges within the measurement window are visible (dashed orange, green, blue, purple traces). (c) Temperature accuracy as a function of averaging time and (d) resolution as a function of noise frequency at 30, 20, 5, and 1 mW laser power levels (blue, orange, green, and red traces, respectively). (e) GeV diamond scanning thermal probe translated in 25 μm steps in the x and y-axes for creation of 2-D thermal images of a heated 120 diameter copper wire. (f) 2-D thermal image of heated copper wire in y- (black squares) and x-axes (red, blue circles) at two locations in the y-axis.

* Reprinted from Blakley, Liu et al. 2019

$\langle \lambda_w \rangle_{T_i}$ is the average λ_w over each T_i, and m is the slope of T_i versus λ_w calculated at the maximum number of samples for each T_i. The slope fit error decreased as a function of n; thus, as the averaging time increased, the accuracy of the thermometer improved. Owing to the enhancement of the SNR, the resolution of these measurements improved as a function of increasing laser power; however, the accuracy only initially improved from 10 K to 700 mK over a 1 Hz bandwidth as the laser power increased from 1 mW to 20 mW and then became worse as the laser power increased to 30 mW (Figure 2.7(c, d)). This is because of laser-induced thermal fluctuations, which introduce deviations from the calibration curve used to ascertain an accurate temperature reading. The temperature resolution of the probe over a 1 Hz bandwidth achieved an optimal value of 20 mK for 20 to 30 mW of laser power or an intensity of 1000 to 1500 W/cm^2. This represents the best temperature resolution for all-optical fiber thermometers described in the literature and remains competitive with free space optical thermometry techniques and microwave-assisted NV thermometers.[1,46,56,74,75]

2.3.3 Spatial resolution of GeV thermometer

To demonstrate this probe's ability to perform high spatial resolution thermal imaging, the diamond was fixed to the fiber with an optical adhesive such that region b was coupled to the core. The diamond was positioned with its sharp edge in the y−z plane suspended above a 120 μm diameter (r) copper wire heated with a 2 A DC current (I) lying along the z-axis (Figure 2.7(e)). The probe was scanned in 25 μm steps along both x- and y-axes. A y-axis temperature calibration curve was produced (Figure 2.7(f), black squares), and an

x-axis temperature profile was created at y-axis displacements of 50 μm and 300 μm (Figure 2.7(f), red and blue circles), producing a 2-D thermal image of the wire with a step-size-limited 25 μm spatial resolution.

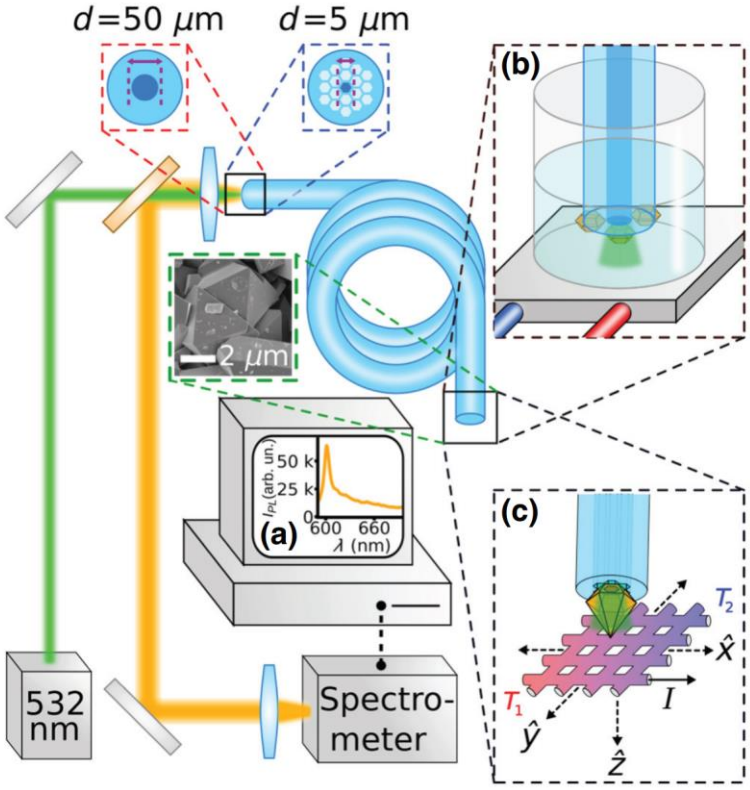

Figure 2.8* The experimental diagram of the Ge-V diamond (dashed green insert) fiber-thermometer probe. (a) The fluorescence spectrum at 50 mW laser power, with a characteristic zero-phonon peak at approximately 601 nm collected by the probe (b), which consists of a Ge-V–microdiamond ensemble affixed to the 50-μm core (dashed red inset) of a step-index fiber. The probe is immersed in a temperature-controlled water bath for sensitivity and calibration measurements. (c) For scanning probe measurements, a F-NL-5/1040 photonic crystal fiber with a 5-μm core (dashed blue inset) is used. An approximately 5-μmdiameter Ge-V microdiamond is affixed to the 5-μm fiber core. The probe tip is scanned in 5-μm steps and temperature measurements are made at each step on the x, y, or z axes in front of various active circuit elements

* Reprinted from Blakley, Vincent et al. 2020

2.4 Photonic Crystal Fiber Probes for Thermal Imaging

As we mentioned before with Figure 2.6(d), we haven't saturated the color centers in diamond. This gives us the opportunity to improve more by decrease the fiber core and diamond size to reach better spiral resolution without losing any sensitivity under same laser power.

In a follow up research work shown in Figure 2.8, we replace the normal index fiber with a photonic crystal fiber for our thermometry probe. By utilizing a photonic crystal fiber (PCF), it is possible to maintain a high numerical aperture (NA) and large numbers of guided modes for enhanced signal collection while reducing the diameter of the fiber core[76], thereby reducing the requisite laser power needed for a given signal amplitude and further reducing the size of the diamond-sensor volume for radically enhanced spatial resolution. This enhanced spatial resolution is necessary for making scanning thermal images of active semiconductor circuit elements and biological tissues at a cellular scale.

CHAPTER 3

DARK EXCITON IN QUANTUM-CONFINED NANOCRYSTALS*

In this chapter, we explore the intense photoluminescence from dark exciton with microsecond lifetime in strongly confined $CsPbBr_3$ nanocrystals and reveal the crucial role of confinement in accessing the dark ground exciton state. We also investigated the size-dependence of the dark exciton photoluminescence properties in $CsPbBr_3$ and $CsPbI_3$ quantum dots in the strongly confined regime, showing the clear role of confinement in determining the bright–dark energy splitting (ΔE_{BD}) and the dark exciton lifetime (τ_D). Those study establishes the potential of strongly quantum-confined perovskite nanostructures as the excellent platform to harvest the benefits of extremely long-lived dark exciton.

3.1 Introduction

3.1.1 Metal Halide Perovskite Nanocrystal

Metal halide semiconductors with perovskite crystal structure have gained much interest as a source of photons due to their facile color tunability and high luminescence quantum yields combined with the relative ease of synthesis.[77-80] For example, cesium lead halide and organic–inorganic hybrid perovskite NCs have been extensively studied as the light emitting component in applications including light emitting devices, single photon emitters, and low threshold nanocrystal-based lasing.[13,81,82] Similar to many other

*Parts of this chapter are reprinted with permission from, Rossi, D. *et al.* Intense Dark Exciton Emission from Strongly Quantum-Confined CsPbBr3 Nanocrystals. *Nano Letters* **20**, 7321-7326, doi: 10.1021/acs.nanolett.0c02714 (2020). Copyright 2021 American Chemical Society. And adapted with permission from, Rossi, D. *et al.* Size-dependent dark exciton properties in cesium lead halide perovskite quantum dots. *The Journal of Chemical Physics* **153**, 184703, doi:10.1063/5.0027972 (2020)

semiconductor NCs, the majority of studies on the photon emission from MHP NCs have focused on the color-tunable exciton emission via chemical control of the bandgap or quantum confinement.[83,84] In addition, photon emission of other origins exhibiting different spectral and dynamic characteristics, such as from luminescent dopants, defects, and self-trapped excitons, was also explored expanding the MHP NC functionality.[85-87]

In this chapter, we will focus on one group of this family, cesium lead halide perovskite, $CsPbX_3$(X=Br, I, Cl). $CsPbX_3$ NC has narrow linewidth with 12nm-40nm, quantum yields reaching 90%.[13] Its photoluminescence (PL) spectrum could cover the entire visible range from 400 nm to 700nm, by continuous tuning of its exciton emission via chemical control of the bandgap such as mixed halide Cl/Br, or quantum confinement.[83,84]

Dark exciton as the lowest-energy (ground) exciton state in metal halide perovskite nanocrystals is a subject of much interest. This is because the superior performance of perovskites as the photon source combined with long lifetime of dark exciton can be attractive for many applications of exciton. However, the direct observation of the intense and long-lived dark exciton emission, indicating facile access to dark ground exciton state, has remained elusive. We will discuss this problem in more detail in next subsection.

3.1.2 Dark Exciton in $CsPbX_3$

The optically inactive dark exciton appears as the lowest energy (ground) exciton state in most semiconductor NCs; therefore, the dark exciton state is populated through the transition from the initially excited bright exciton to dark exciton state. At low temperatures with thermal energy (kT) smaller than the bright−dark energy splitting

(ΔE_{BD}), a substantial dark exciton population can be obtained giving rise to long-lived photoluminescence (PL) from the radiative relaxation of dark excitons.[88-90]

Recently, the reversal of the bright and dark exciton level ordering was reported in cesium lead halide ($CsPbX_3$) NCs, based on the observation of only bright exciton PL in single-particle studies at cryogenic temperatures, indicating the loss of the typical pathway to reach the dark exciton level.[16] On the other hand, a study in $FAPbBr_3$ NCs under magnetic field reported the signature of a dark exciton ~2.5 meV below the bright exciton level in the single-particle PL spectra.[17] Another study in Mn-doped $CsPbCl_3$ NCs also argued for the dark ground-state exciton from the observation of the weak but longer-lived decay component in the lower-temperature PL.[91] However, because of the dominance of the bright exciton PL even at cryogenic temperatures and the absence of a direct measurement of the dark exciton relaxation, the accessibility to dark exciton as well as its energetic and dynamic characteristics still remains elusive in this new class of semiconductor NCs. In Section 3.2, we will demonstrate the observation of dark ground exciton. The key element of successful access to dark exciton emission is quantum confinement, which we will introduce following

3.1.3 Quantum Confinement in $CsPbX_3$

In bulk semiconductor, an exciton has a radius associated with it call Bohr radius. When the nanocrystal size is smaller than Bohr diameter, the electric state will change with nanocrystals' size, this is called the quantum confinement effect. The overlap of

wavefunction of electron and hole will enhance their exchange interaction, which directly result in exciton fine structure.

In the case of $CsPbX_3$, dark bright exciton splitting or the fine structure of exciton is also originate from electron-hole exchange interaction (EI), where original degenerate states split into one triplet state (bright exciton) and one singlet state (dark exciton).[92] The Hamiltonian of this EI is $H_{exch} = -\alpha_{exc}\Omega_0(\sigma^e \cdot \sigma^h)\delta(r_e - r_h)$ where $\sigma^{e,h}$ are electron and hole Pauli operator, α_{exc} is the exchange strength, and Ω_0 is the volume of the unit cell.[16] One can show that the splitting between triplet and singlet state is 4η where $\eta = 4\Theta$, and $\Theta = \int v^2(r,r)d^3r$, where $v(r_e, r_h)$ is the envelope function of exciton. In strong confined regime $\Theta \sim \Omega_0/V$, which is inverse proportional to the nanocrystal volume, whereas in weak confined regime or bulk $\Theta = \Omega_0/\pi a_B^3$. This is consistent with previous study that the splitting will be enhanced by stronger quantum confinement.[93] In bulk CdSe, the exchange energy is just 0.13meV,[19] while in the quantum confined region, the exchange energy in CdSe is in the order of 10meV.[93 94] There is also study tuning the dark bright exciton splitting by varying the CdSe/CdS NCs shell width.[19]

The Bohr diameter for $CsPbBr_3$ is 7nm, and 12nm, 5nm for $CsPbI_3$, $CsPbCl_3$ respectively.[80] So our 4nm $CsPbBr_3$ is in strong quantum confinement region. In next section, we will demonstrate the critical role of quantum confinement in access to the dark exciton emission.

3.2 Intense Dark Exciton Emission from Strongly Quantum-Confined $CsPbBr_3$ Nanocrystals

In this section, we report the direct observation of intense and long-lived PL with 1−10 μs lifetime from dark ground exciton state in strongly quantum-confined $CsPbBr_3$ NCs revealing the importance of confinement-enhanced ΔE_{BD} in gaining facile access to dark exciton. In contrast to MHP NCs studied earlier that were in the weak confinement regime, strongly quantum confined $CsPbBr_3$ NCs at cryogenic temperatures exhibit the PL primarily from dark exciton. The ΔE_{BD}, determined directly from the PL spectra, is significantly larger than weakly confined $FAPbBr_3$ NCs and strongly confined NCs of many other semiconductors.[17,90,95-97] The larger ΔE_{BD} in strongly confined $CsPbBr_3$ NCs enables access to the dark exciton at higher temperatures, which is particularly important for the applications of dark exciton.

3.2.1 Different Dimensionality of the Confinement on Nanocrystal

Although a lot of studies related to quantum confinement have focus on quantum dots, where the exciton is in 3-dimensional confinement, enhanced electron-hole exchange interaction could still be observed in 2-dimensional confined nanowire, and 1-dimensional confined nanoplatelet. To demonstrate that, in the experiment of this section, we use four types of $CsPbBr_3$ nanocrystals. Figure 3.1 shows the electron microscopy images and room temperature optical spectra of weakly confined NCs and strongly confined quantum dots (QDs), nanowires (NWs), and nanoplatelets (NPLs) of $CsPbBr_3$ used to examine the PL from dark exciton. The size of the NCs in the quantum confined

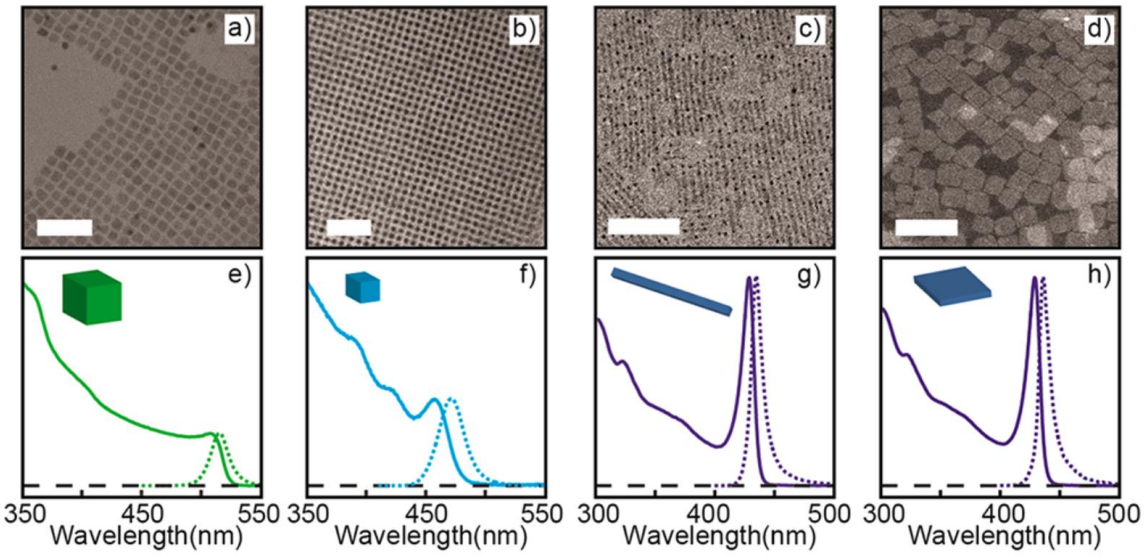

Figure 3.1* Electron microscopy images (a−d) and optical spectra (e− h) of weakly confined NCs (l = 10 nm) and strongly confined QDs (l = 4 nm), NWs (l × w = 2 × 100 nm), and NPLs (l × w × h = 2 × 25 × 25 nm), (left to right). The cartoon depicting the NC morphology and the size are indicated in each panel. Solid and dashed lines in the spectra are for the absorption and photoluminescence, respectively. (a−c) TEM images; (d) STEM image. Dark spots in (c) are formed during TEM imaging likely from the e-beam damage of the NWs. TEM scale bars (a−c) 50 nm (d) 100 nm.

dimension indicated in Figure 3.1 for the QDs, NWs, and NPLs is much smaller than twice the exciton Bohr radius of $CsPbBr_3$ ($2a_B$ = 7 nm) imposing strong quantum confinement in varying dimensionality.[80] The weakly confined NCs were prepared following the procedure reported by Protesescu et al.[80] Strongly confined QDs, NWs, and NPLs were synthesized following the methods developed by Dong et al. which can control the size and morphology precisely with high ensemble uniformity, as reflected in the microscopy images and the optical spectra showing the well-defined features of strongly confined excitons.[84,98] For the optical measurements, all of the samples were passivated with dimethyl-dioctadecyl-ammonium bromide (DDAB) via ligand exchange for improved

*Reprinted from Rossi, Liu et al. 2020

stability and PL quantum yield in polystyrene (PS) matrix used to disperse the NCs for PL measurements.

3.2.2 Time-resolved PL Spectra at 5K

To obtain the direct information about dark exciton, our coworker Denial have implemented a series of the time resolved PL measurement as discussed in this subsection. Figure 3.2 shows the time-resolved PL spectra (a−d), spectrally integrated PL decay dynamics (e−h), and steady state PL spectra (i−l) following above-bandgap excitation (400 or 405 nm) at 5 K for the four $CsPbBr_3$ NC samples shown in Figure 3.1. While the PL spectra at 300 K exhibits a single well defined PL feature which decays on the several ns time scale for all samples, at 5 K the PL shows very different spectral and dynamic features. In the weakly confined CsPbBr3 NCs, a single PL peak with ∼500 ps decay time is observed (Figure 3.2a,e,i), similar to the results from earlier studies performed at either single-particle or ensemblelevel.[16,99,100] Because of the intense and fast-decaying PL on the sub nanosecond time scale even at 5 K, a recent study by Becker et al. concluded that the dark exciton level is above the bright exciton level which dominates the 5 K PL in $CsPbBr_3$ NCs.[16] On the other hand, a study by Chen et al. concluded that the dark exciton is below the bright exciton level based on the kinetic analysis of the temperature-dependent PL dynamics, although the accuracy of the kinetic model for extracting the relevant parameters needs further scrutiny.[101] In another study by Canneson et al., the same sub nanosecond PL observed at 5 K from CsPbBr3 NCs was interpreted as the negative trion PL arising from a charged subpopulation of NCs, with little contribution from the

neutral (bright exciton) subpopulation of the NCs.[100] Despite the differences in the interpretation of the PL in different studies, all converged on very weak or lack of dark exciton PL in weakly confined $CsPbBr_3$ NCs.

In contrast, all three strongly confined NCs of varying dimensionalities, that is, QDs, NWs, and NPLs, exhibit two different PL peaks with decay time constants that differ by many orders of magnitude (Figure 3.2b−d). Time gating the PL spectra near 0 ps and 0.5 μs readily reveals the two PL peaks separated by 17−22 meV as shown to the right of Figure 3.2b− d. The fast and slow components of the PL decay kinetics in Figure 3.2f−h with corresponding time constants of τ_{fast} and τ_{slow} are associated with the higher-energy and lower-energy PL peaks, respectively. Fitting the steady-state PL spectra (Figure 3.2j−l) with the two PL peaks indicates that the lower-energy PL constitutes ∼70% of the total photons emitted at 5 K in these NCs.

We assign the higher-energy and lower-energy PL to the bright and dark excitons respectively, as will be discussed in detail shortly. Since the bright and dark exciton PL are clearly separable in the time-resolved spectra, ΔE_{BD} is directly determined from the separation between the two PL peaks. Table 3-1 summarizes ΔE_{BD}, τ_{fast}, and τ_{slow} of the PL decay kinetics, and the fraction of photons from the dark exciton in the PL at 5 K. Since ΔE_{BD} is much larger than kT at 5 K, prohibiting thermal excitation from the dark to bright exciton states, τ_{slow} can reliably be taken as the dark exciton lifetime τ_D. On the other hand, τ_{fast} reflects the decay of the bright exciton population via radiative and nonradiative relaxation combined with transition between the bright to the dark exciton states.

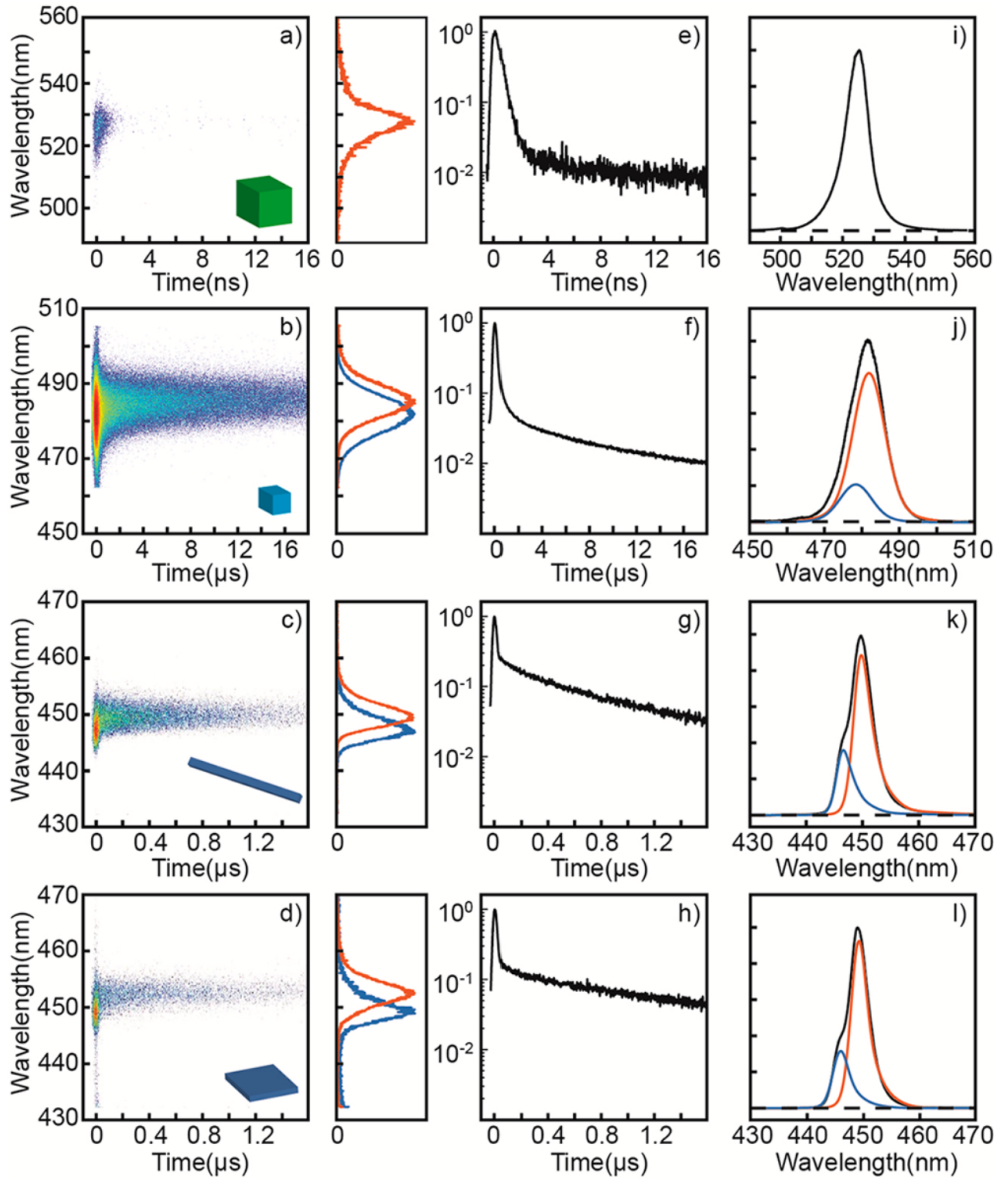

Figure 3.2* Time-resolved PL spectra (a–d), normalized spectrally integrated PL decay dynamics (e–h), and steady-state PL spectra (i– l) of four different $CsPbBr_3$ NCs measured at 5 K. The data are for weakly confined NCs, QDs, NWs, and NPLs from top to bottom. The two spectra shown next to panels b-d are the time-gated PL spectra taken near 0 ps (blue) and 0.5 μs (red). These two spectra are used to fit the steady-state spectra in (i–l).

*Reprinted from Rossi, Liu et al. 2020

The estimation of the bright exciton lifetime (τ_B) and the time constant for the bright-to-dark transition (τ_{BD}) has been made from the analysis of the relative intensities of the bright and dark exciton PL at 5K with a few assumptions, as described in detail in the Appendix C.

In Table 3-1, τ_{BD} is significantly shorter than τ_B for all three strongly confined NCs, indicating that dark exciton can be reached effectively from the initially excited bright exciton. This contrasts to the conclusions from the earlier study in organic−inorganic hybrid $FAPbBr_3$ NCs that also have ground dark exciton level with ΔE_{BD} of 2−3 meV but does not show dark exciton PL in the absence of magnetic field.[17] It was considered that slow bright-to-dark transition is responsible for the difficulty in observing dark exciton PL in the MHP NCs. The present study suggests that the confinement-enhanced ΔE_{BD} is a more critical factor that determines the accessibility to the dark exciton in $CsPbBr_3$ NCs. The confinement enhancement of ΔE_{BD} was predicted earlier from a theoretical study and is consistent with the variation of ΔE_{BD} at 5 K in QDs and NPLs with the degree of quantum confinement observed in this study.[92,102]

It is worth noting that ΔE_{BD} of $CsPbBr_3$ QDs and NPLs are significantly larger than ΔE_{BD} of CdSe QDs and NPLs of similar size and thickness, whose exciton fine structure was extensively studied as a prototypical semiconductor NC system. For CdSe QDs, ΔE_{BD} of 0.8−6 meV was reported for QDs of ~4 nm in diameter and ΔE_{BD} of 12.5 meV for QDs of 2.4 nm in diameter.[93,96,97] ΔE_{BD} of 2−4.5 meV was reported for CdSe NPLs of 1.2−1.5 nm in thickness in the literature.[95] Interestingly, τ_B of NWs (160 ps) and NPLs (124 ps) is nearly an order of magnitude shorter than in QDs. The faster τ_B in NWs and NPLs

compared to QDs is reminiscent of the enhanced exciton recombination rate observed in other 1D and 2D confined semiconductors, reflecting the larger exciton binding energies and enhanced electron−hole correlations.[95,103] Despite the rapid relaxation of bright exciton in NWs and NPLs, even more rapid bright-to-dark transition enables reaching dark exciton as efficiently as in QDs.

Table 3-1* Parameters Extracted from the PL Decay Data at 5K

Sample	ΔE_{BD}	τ_{slow}	τ_{fast}	τ_B	τ_{BD}	I_D/I_{tot}
QD	17	10	387	1600	510	76
NW	19	0.85	44	160	62	68
NPL	22	1.2	37	124	54	73

3.2.3 Assign Microseconds-lived Lower-energy PL to Dark Exciton

The assignment of microseconds-lived lower-energy PL to the dark exciton has been made by ruling out other processes that can produce a PL red-shifted from the bright exciton PL in MHP NCs and performing the magneto fluorescence measurements. Self-trapped exciton, phonon replica, and defect emission have been discussed previously as the origin of redshifted PL observed in several MHP materials both in bulk and nanocrystalline forms.[86,104-107] In addition, trion emission or interparticle excimer-like emission has been discussed as the origin of certain PL features red-shifted from the exciton PL in CdSe NPLs and in weakly confined CsPbBr3 NCs.[108-110] These alternative possibilities were

*Reprinted from Rossi, Liu et al. 2020

ruled out by examining the difference in the spectral characteristics of the PL, such as the linewidth, lifetime, the magnitude of red shift from the bright exciton, and the dependence of the lifetime on external magnetic field.

Self-trapped exciton has been discussed extensively to explain a broad PL feature red-shifted from the exciton PL observed in some MHP NCs prominent under the sub gap excitation condition.[107] PL from the self-trapped exciton typically has a much larger spectral line width and Stokes shift than the exciton PL due to the larger lattice displacement associated with these transitions. In $CsPbBr_3$ NCs, the PL from self-trapped exciton was observed ~100 meV below the exciton PL with a three times broader line width and a lifetime of ~170 ns, very different from the lower-energy PL observed in the strongly confined $CsPbBr_3$ NCs of this study. Furthermore, the disappearance of the self-trapped exciton PL with above-bandgap excitation further rules out self-trapped exciton as the origin for the microseconds-lived lower-energy PL observed in our study. Similarly, phonon overtones are observed in the low-temperature PL spectra for all semiconductors. The first phonon overtone will appear as a PL sideband red-shifted by one optical phonon energy with an intensity proportional to the exciton−phonon coupling. While ΔE_{BD} in this study is similar in the order of magnitude to the optical phonon energy of bulk $CsPbBr_3$, the large disparity between the lifetimes of the two PL peaks by many orders of magnitude immediately dismisses this possibility.

A red-shifted PL feature with similar spectral line width to the exciton PL is often observed in the low-temperature PL spectra of CdSe NPLs. While its origin is still debated, two recent works suggested it may result from the excimer-like emission from stacked NPLs

or trion emission.[109,110] Considering that we observed the red-shifted PL universally in all strongly quantum-confined NCs of different dimensionalities, the excimer-like emission observed in CdSe NPLs is not likely to explain our observation in MHP NCs. Trion PL red-shifted from neutral bright exciton PL, reported in weakly confined $CsPbBr_3$ NCs, has sub nanoseconds decay time many orders of magnitude shorter than μs decay time of the lower-energy PL in this study.[108] Furthermore, the independence of the PL lifetime on the magnetic field from these two origins contrasts with the strongly magnetic field-dependent lifetime of the slow-decay component in the PL shown in Figure 3.3, further ruling out these two options.

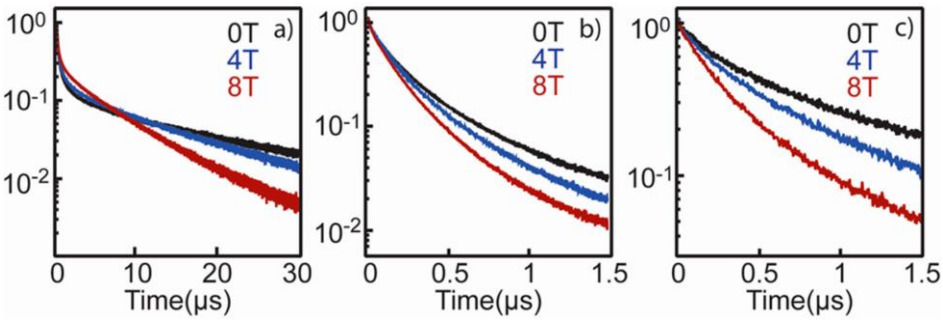

Figure 3.3* Magnetic field-dependent PL decay dynamics of $CsPbBr_3$ QDs (a), NWs (b), and NPLs (c) at liquid helium temperature. Only the slow-decay component of the PL decaying on a microsecond timescale is plotted for NWs and NPLs since 150 ns excitation pulse interferes with correct interpretation of the fast component decaying in <50 ps. For QDs with ~400 ps fast-decay component, the entire PL decay kinetics are shown

3.2.4 Magnetic Field Dependent PL

Figure 3.3 shows the dependence of the slow-decay component of the PL from $CsPbBr_3$ QDs, NWs, and NPLs under 0T, 4T, and 8T magnetic field at liquid helium temperature.

*Reprinted from Rossi, Liu et al. 2020

For all three of the strongly confined NCs, the lifetime of the slow-decay component assigned to dark exciton PL shortens with increasing magnetic field. The shorting of the lifetime is consistent with the expected behavior of the dark exciton, which results from the mixing of the bright and dark state by the magnetic field. The physics mechanism is described in detail in Appendix C. The similar trend of magnetic field dependence of the dark exciton lifetime was observed in recent studies on single $FAPbBr_3$ NCs and Mn-doped $CsPbCl_3$ NC ensembles.[17,91] For self-trapped exciton, defect emission, trion emission, and excimer-like emission, the dependence of the PL lifetime on the magnetic field is not expected, as has been experimentally confirmed in several studies.[109,110] In addition to the discussion above, the shortening of the PL lifetime under the magnetic field supports decisively the assignment of the lower-energy PL with 1−10 μs lifetime to the dark exciton

3.2.5 Temperature-Dependent τ_{fast} and τ_{slow}

To gain further insights into the competitive dynamics of the exciton relaxation and bright-to-dark transition and to check if parameters in Table 3-1 determined from the spectra at 5 K are valid beyond 5 K, the temperature dependent τ_{fast} and τ_{slow} were analyzed with a kinetic model as shown Figure 3.4. Under this simple kinetic model, τ_{fast} and τ_{slow} at each temperature are determined by the competition of the relaxation of bright and dark excitons separated by ΔE_{BD} and the temperature-dependent reversible transition between bright and dark states as explained in detail in Appendix C. Often, ΔE_{BD} and time constants (τ_B, τ_D, and τ_{BD}) are extracted as the best fitting parameters of the temperature dependent

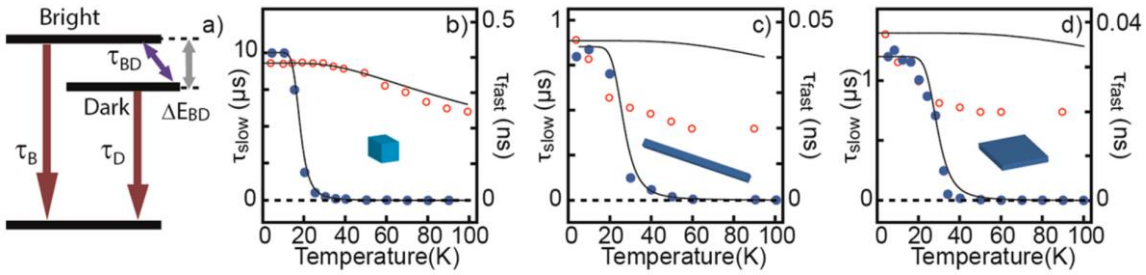

Figure 3.4* Kinetic model (a) used to analyze the temperature dependence of τ_{fast} (○) and τ_{slow} (●) from QDs (b), NWs (c), and NPLs (d). Curves are the values calculated using the kinetic model and nonadjustable parameters in Table 3-1

τ_{fast} and τ_{slow} to the kinetic model, when these cannot not be directly determined from the time-resolved spectra unlike in this study.[91,97,100,111] If the kinetic model accounts for all the dynamic processes in the NCs studied here ideally, the model should reproduce τ_{fast} and τ_{slow} from the ΔE_{BD} and time constants in Table 3-1. Figure 3.4b−d compares τ_{fast} and τ_{slow} of QDs, NWs, and NPLs with the calculated values using the model in the temperature range of 5−100 K. The details of calculation are in Appendix C. For QDs, the temperature dependence of τ_{fast} and τ_{slow} are well reproduced with the kinetic model using ΔE_{BD}, τ_B, τ_D, and τ_{BD} in Table 3-1 as nonadjustable parameters up to 100 K. This indicates that the kinetic model is reasonably satisfactory for describing the exciton dynamics in QDs and that ΔE_{BD} and the time constants determined from 5K spectra are valid in the higher temperature ranges. The same analysis for NWs and NPLs reproduces τ_{slow} quite well, while τ_{fast} shows more discrepancy between the measured and calculated values from the model. The rapid change of the experimentally measured τ_{fast} in 5−20 K suggests the

*Reprinted from Rossi, Liu et al. 2020

possible involvement of an additional nonradiative decay channel for the exciton in NWs and NPLs that is not accounted for in the kinetic model employed here. Since τ_{fast} is more sensitive to τ_B and τ_{BD} than to τ_D, the temperature dependence of τ_B is the most likely culprit. The larger discrepancy of the measured and calculated τfast in NWs and NPLs compared to the QDs is also consistent with the more complicated and larger temperature dependence of the relative PL QY in NWs and NPLs (Figure 4.3).

3.3 Size-dependent Dark Exciton Properties in $CsPbX_3$

In previous section, we described the observation of the intense and long-lived dark exciton PL from $CsPbBr_3$ NCs at cryogenic temperatures when strong quantum confinement is imposed. An important difference between the strongly and weakly confined $CsPbBr_3$ NCs recognized from our study was the larger ΔE_{BD} in more strongly confined QDs that played a crucial role in giving more facile access to the intense and long-lived dark exciton PL. In fact, theoretical studies predicted that quantum confinement dictates ΔE_{BD} via the size-dependent electron–hole exchange energy resulting in the increasing ΔE_{BD} with the decreasing QD size.[92] Furthermore, earlier studies on CdSe QDs indicated that the size-dependent ΔE_{BD} affects the lifetime of dark excitons (τ_D) as well.[97] To obtain a more detailed picture of the behavior of the dark exciton in strongly confined cesium lead halide ($CsPbX_3$) perovskite QDs, in this section we describe our investigation of the size-dependence of ΔE_{BD} and dark exciton lifetime (τ_D). Two different systems ($CsPbBr_3$ and $CsPbI_3$ QDs) were studied in this work, which showed the common trend in the size-dependence of both ΔE_{BD} and τ_D, consistent with the earlier predictions.

The results of this study provide an important insight into the role of quantum confinement in determining the characteristics of the low-temperature PL and access to the long-lived dark exciton, which will be important in the future application of dark excitons

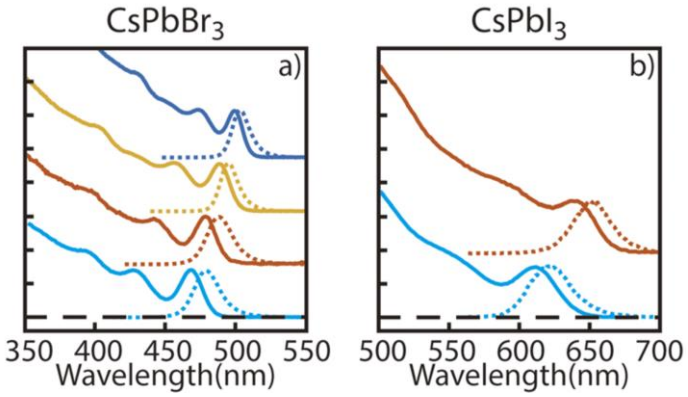

Figure 3.5* Room-temperature absorption (solid lines) and PL (dashed lines) spectra of (a) $CsPbBr_3$ QDs (l = 3.9 nm, 4.8 nm, 5.6 nm, and 6.5 nm from bottom to top) and (b) $CsPbI_3$ QDs (l = 4 nm and 6.5 nm from bottom to top) dispersed in hexane

3.3.1 Sample Size of $CsPbBr_3$ and $CsPbI_3$ QDs

Figure 3.5 shows the room-temperature steady-state absorption and PL spectra of $CsPbBr_3$ and $CsPbI_3$ QDs of different sizes in the strongly quantum confined regime, which were used to examine the size-dependence of the dark exciton PL. Both $CsPbBr_3$ and $CsPbI_3$ QDs are in the strongly confined regime, where the edge length (l) is smaller than twice the exciton Bohr radius (r_{Bohr}); r_{Bohr} = 3.5 nm and 6 nm for CsPbBr3 and CsPbI3, respectively.[80] The edge length (l) of the QDs and the room-temperature PL peak wavelength (λ_{pl}) are listed in Table 3-2. The absorption spectra of the QDs show well defined confined exciton absorption peaks of the first few excitonic transitions, reflecting

*Reprinted from Rossi, Qiao et al. 2020

high ensemble uniformity of the QDs synthesized employing the equilibrium-based size control.[84]

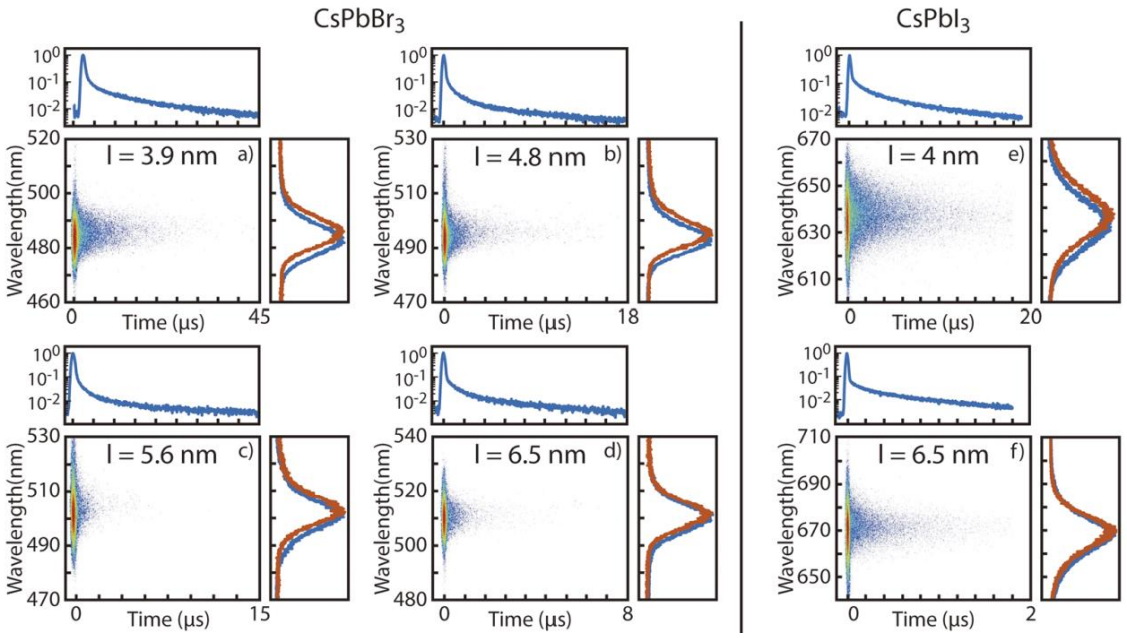

Figure 3.6* Time-resolved PL spectra from [(a)–(d)] $CsPbBr_3$ and [(e)–(f)] $CsPbI_3$ QDs at 5 K. The QD size (edge length) is shown in each panel. Time-gated normalized PL spectra near 0 ns (blue) and 500 ns (red) are shown on the right of each panel, which are used to extract ΔE_{BD}. The time-dependent total PL intensity is shown above the time-resolved PL spectra

3.3.2 Time-resolved PL Spectra

Figure 3.6 shows the time-resolved PL spectra from the different sized $CsPbBr_3$ [(a)–(d)] and $CsPbI_3$ [(e)–(f)] QDs at 5 K obtained with a streak camera after the pulsed excitation (45 ps pulse width) at 405 nm. All the QDs exhibit two distinct spectral features, i.e., higher-energy PL with the faster decay time constant (τ_{fast}) on the sub-ns timescale and the lower-energy PL with the slower decay time constant (τ_{slow}) on the >μs timescale. The

*Reprinted from Rossi, Qiao et al. 2020

two distinct PL decay times are more clearly seen in the time-dependent total PL intensity plotted above each time-resolved PL spectrum. The spectral separation of the higher-energy PL with the decay time constant fast and the lower-energy PL with the decay time constant τ_{slow} was achieved by taking the time-gated PL near 0 ns and 500 ns. The spectrally separated and normalized PL spectra obtained from this procedure are shown on the right side of each time resolved PLs spectrum.

The two important size-dependent properties of dark exciton PL we focus on in this study are the bright–dark splitting energy(ΔE_{BD}) and dark exciton lifetime (τ_D), which are listed in Table 3-2. The method to extract those parameters are discussed in detail at Appendix C. For both CsPbBr3 and CsPbI3 QDs, ΔE_{BD} increases with the decreasing QD size and τ_D was increases with the decreasing QD size. We will discuss the origin of those in more detail in next part. Table 3-2 also shows the size-dependence of three other quantities: τ_B, τ_{BD}, and the fraction of dark exciton PL in the total PL intensity (I_D/I_{tot}) at 5 K.

3.3.3 Validation of Dark Exciton Picture

Before we dive into the discussion of dark exciton properties, we first verify our dark exciton picture with those QDs. To do that, we implemented magnetic field and temperature dependent PL measurement. As we discuss in previous section, PL red-shifted from the bright exciton PL can be observed from several different sources, such as self- trapped excitons, phonon replicas, defect emission, and trion emission in various semiconductor NCs.[86,104-107] However, these possibilities were each ruled out based on

Table 3-2* Edge length of the QD (l), room-temperature PL peak wavelength (λ_{pl}), bright–dark splitting energy (ΔE_{BD}), dark exciton lifetime (τ_D), bright exciton lifetime (τ_B), bright-to-dark transition time (τ_{BD}), and relative intensity of dark exciton PL to total PL intensity (I_D/I_{tot}) at 5 K determined from the time-resolved PL spectra shown in Figure 3.6

Sample	l(nm)	λ_{pl}	ΔE_{BD} (meV)	τ_D (μs)	τ_B (ps)	τ_{BD} (ps)	I_D/I_{tot}
$CsPbBr_3$	3.9	479	17	14	510	490	0.63
	4.8	488	8	9	62	890	0.45
	5.6	495	5	4.5	54	1700	0.25
	6.5	501	3.5	2.5	…	…	0.2
$CsPbI_3$	4	627	7.5	6	2600	1000	0.73
	6.5	648	2	1.3	1600	1400	0.52

the spectral linewidth and lifetime, as well as the shortening of τ_D under the magnetic field. The magnetic mixing of bright and dark excitons evidenced by shortening of long component lifetime as shown in Figure 3.7, can be explained only by dark excitons. Therefore, the time-resolved PL spectra of all $CsPbBr_3$ and $CsPbI_3$ QDs in Figure 3.6, exhibiting the same two separable. spectral features, can be interpreted in the same way, allowing for the systematic study of the effect of varying size on the properties of dark excitons.

The temperature-dependence of τ_{slow} is also analyzed with the three-level kinetic model shown in Figure 3.8(a), which describes the competitive dynamics of bright and dark exciton relaxation in the presence of thermal equilibration between them.[97,112]

*Reprinted from Rossi, Qiao et al. 2020

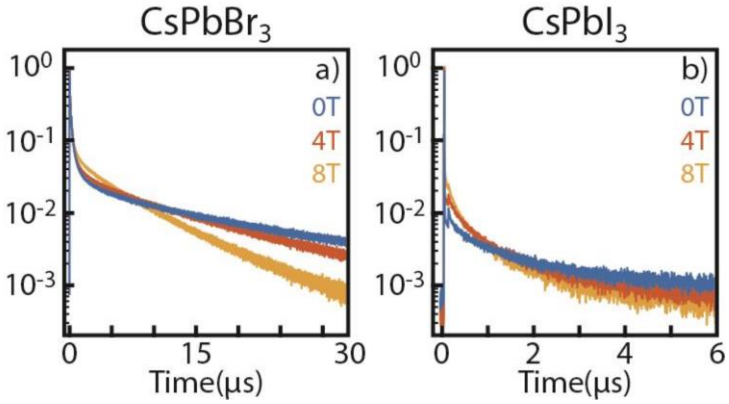

Figure 3.7* Time-dependent PL decay at 5K under magnetic field of 0T, 4T, and 8T for a) 4 nm $CsPbBr_3$ QDs and b) 6.5 nm $CsPbI_3$ QDs

This analysis will further confirm the validity of the physical picture (three-level kinetic model) in understanding the temperature-dependent dark exciton PL and the values of τ_D and ΔE_{BD} determined directly from the 5 K spectra. The detailed description of the kinetic model and calculation of the temperature-dependent τ_{slow} are in the Appendix C. Figure 3.8(b) and Figure 3.8(c) compare the temperature-dependence of ΔE_{BD} for $CsPbBr_3$ and $CsPbI_3$ QDs of different sizes. Markers are the experimentally determined values. The curves superimposed on the experimental data are the calculated temperature-dependent τ_{slow}. The experimentally measured $\tau_{slow}(T)$ fits very well to the simple three-level kinetic model for $CsPbBr_3$ and $CsPbI_3$ QDs of all the sizes studied here using the nonadjustable parameters determined from the time-resolved PL spectra at 5 K shown in Table 3-2. This indicates that the size-dependent ΔE_{BD} and τ_D of the QDs are fully consistent with the thermally equilibrating bright and dark exciton picture described by the three-level kinetic model.

*Reprinted from Rossi, Qiao et al. 2020

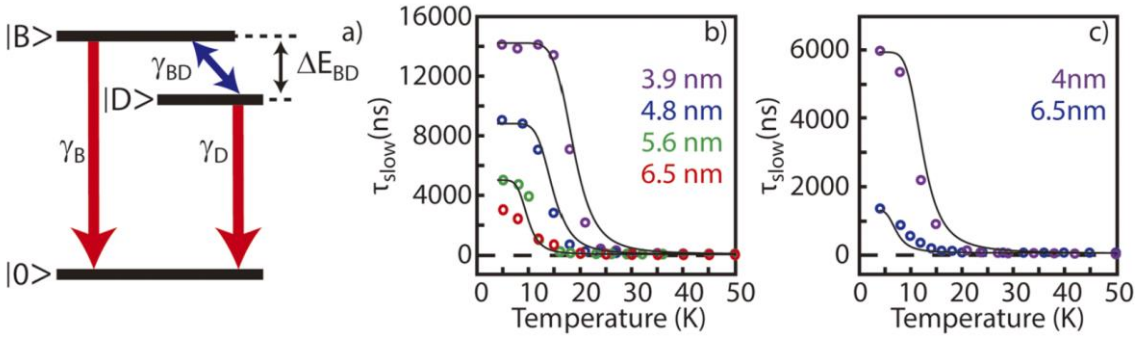

Figure 3.8* (a) Three-level kinetic model describing the equilibration between the bright and dark excitons. Temperature dependence of τslow for $CsPbBr_3$ (b) and $CsPbI_3$ (c) QDs of varying sizes. Markers are the experimental data, and solid curves are calculation using kinetic mode describe in Appendix C

3.3.4 Size Dependent Electron-hole Exchange Energy

Having established the reliability of ΔE_{BD} and τ_D determined from the 5 K spectral data, which can describe the temperature dependence of τ_{long} very well with the three-level kinetic model, we examine their size-dependence and discuss the role of quantum confinement. Earlier theoretical studies on $CsPbBr_3$ NCs by Sercel et al. predicted the increasing ΔE_{BD} with increasing quantum confinement.[92] In their study, the confinement enhanced ΔE_{BD} was modeled using the effective mass calculations including both short and long range exchange coupling, crystal field strength, Ashba splitting, and particle asymmetry.[92] For weakly confined NCs, these calculations predict the lowest-energy exciton level to be a bright exciton, which is opposite to most known semiconductor NCs where the lowest-energy exciton state is dark. However, the switching of the bright–dark level order in the smaller particles together with the increase in ΔE_{BD} with the decreasing QD size was also predicted. In their study, ΔE_{BD} is influenced by not only the size-

*Reprinted from Rossi, Qiao et al. 2020

dependent electron–hole exchange energy that increases with increasing quantum confinement but also the crystal field (e.g., cubicor tetragonal) and the particle shape anisotropy.

While it is difficult to estimate the relative importance of each factor in determining the size-dependence of ΔE_{BD}, we consider that the size-dependent electron–hole exchange energy that scales with the inverse particle volume ($1/l^3$) of the QDs is the major factor.[92] This hypothesis is supported by the plot of ΔE_{BD} vs $1/l^3$ for the case of $CsPbBr_3$ QDs shown in Figure 3.9(a), which shows the linear increase in ΔE_{BD} with $1/l^3$. The effects of the exchange coupling are also consistent with the smaller ΔE_{BD} for $CsPbI_3$ with comparably sized $CsPbBr_3$. Despite the larger exciton Bohr radius of $CsPbI_3$, which suggests stronger confinement, it has been reported that $CsPbI_3$ has a weaker exchange interaction, resulting in the smaller ΔE_{BD}.[16] While our size-dependent ΔE_{BD} data are limited to a smaller set of samples for $CsPbI_3$ QDs, the same trend of size-dependence is observed universally in both $CsPbBr_3$ and $CsPbI_3$ QDs.

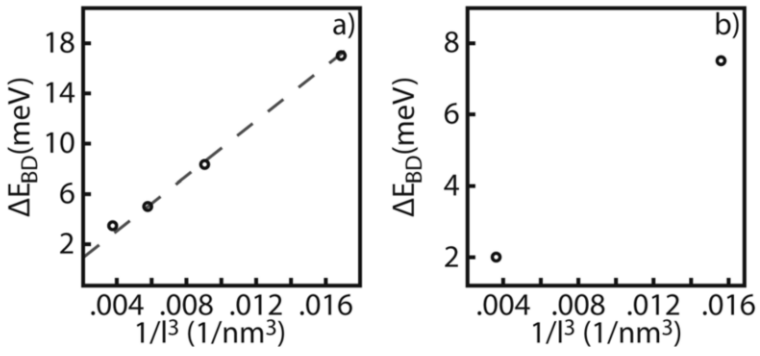

Figure 3.9* Size-dependent ΔE_{BD} vs $1/l^3$ for $CsPbBr_3$ (a) and $CsPbI_3$ (b) QDs. The dashed line is a visual guide

*Reprinted from Rossi, Qiao et al. 2020

The dark exciton lifetime (τ_D) also shows the strong dependence on the size of the QDs. For both $CsPbBr_3$ and $CsPbI_3$ QDs, τ_D increases with increasing confinement, likely reflecting the decreased dark exciton oscillator strength if quantum yield of radiative decay of the dark exciton does not vary significantly with the size of the QDs. The origin of the dark exciton oscillator strength in QDs is complex and has been studied extensively in II–VI QDs, which will be discussed in more detail below.[113-117] In most semiconductor QDs, the finite dark exciton oscillator strength of the formally forbidden dark exciton transition is explained through several perturbations that can mix in other states with allowed transitions into the new eigenstate. For instance, the magnetic field can mix the bright and dark states providing enhanced oscillator strength to the dark exciton, which has allowed for the observation of dark exciton PL more readily in many QDs where the dark exciton PL is otherwise unobservable.[113] The magnetic field enhanced oscillator strength also manifests the reduced dark exciton lifetime(τ_D).[17,118] Both $CsPbBr_3$ and $CsPbI_3$ QDs studied here exhibit shortening of τ_D under the magnetic field as expected from the magnetic mixing of bright and dark excitons.

In the absence of the magnetic field, other perturbations should account for the finite dark exciton oscillator strength that enables the observation of dark exciton PL. In the case of the extensively studied CdSe QDs, a number of mechanisms have been suggested to explain the finite oscillator strength of the dark exciton. For example, surface/defect spins or acoustic/optical phonons were proposed to provide pathways of satisfying momentum conservation necessary for radiative relaxation of dark excitons.[113-117] Other factors, such as spin–orbit coupling, were also considered possible perturbations to mix bright and dark

exciton states.[119] There is strong evidence for both phonon assisted and surface spin mechanisms, and multiple studies have suggested that both can contribute to the oscillator strength of dark excitons in CdSe QDs depending on the QD size and temperature.[96,118]

In the case of MHP perovskite NCs, little has been discussed in the literature about the specific mechanism giving oscillator strength to the dark exciton since the earlier works that studied only the weakly confined NCs did not observe dark exciton PL without the external magnetic field. Therefore, it was considered intrinsically non-emissive in the absence of the magnetic field, even if it may be the lowest-energy exciton state, due to the lack of mechanisms to activate it.[102] In contrast to these earlier observations in weakly confined NCs, dark excitons in strongly confined QDs are clearly emissive, and τ_D varies clearly with the QD size. Presently, what specific mechanism is operating to give dark exciton oscillator strength is unclear and will require further experimental and theoretical studies. Nevertheless, the increasing τ_D with increasing quantum confinement may be explained by less efficient mixing of dark and bright states by the perturbation giving the oscillator strength with the increasing ΔE_{BD}. The same explanation was given previously for the case of CdSe QDs, which may be equally valid in MHP NCs.[119]

From the practical point of view of QDs as the source of photons, smaller $CsPbBr_3$ and $CsPbI_3$ QDs exhibit stronger dark exciton PL indicating more facile access to the emitting dark exciton state. The accessibility of dark exciton PL at cryogenic temperatures is affected by not only ΔE_{BD} dictating the thermal equilibration between bright and dark states but also τ_B and τ_{BD} determining the branching of the emitting state between bright and dark excitons. Interestingly, τ_B decreases with the increasing QD size, potentially

indicative of the larger oscillator strength in the large QDs. It has been previously suggested that the larger $CsPbX_3$ NCs gain more oscillator strength via giant oscillator strength transitions.[16] While additional evidence is required for a more definitive proof, our observation of decrease in τ_B with the increasing QD size is consistent with their explanation. Table 3-2 shows that τ_{BD} also increases with the increasing QD size. The bright–dark relaxation(τ_{BD}) typically involves the absorption or emission of phonons to account for ΔE_{BD}. In the case of CdSe QDs, this process is considered to involve the emission of a single acoustic phonon.[117] In contrast, in weakly confined $FAPbBr_3$ and $FAPbI_3$ NCs, the simultaneous absorption and emission of two optical phonons with an energy difference equal to ΔE_{BD} were proposed due to the large mismatch between the acoustic/optical phonon energy and ΔE_{BD}.[17,104] We suspect the faster τ_{BD} in the smaller particles observed here results from the increase in ΔE_{BD}, which more closely matches the LO phonon energy allowing for the more efficient single phonon emission. Further studies will be necessary to gain a more complete understanding of the size-dependence of the bright–dark transition rate in $CsPbX_3$ QDs.

CHAPTER 4

CONCLUSIONS

In conclusion, for all optical thermometry based on group IV color center, we first reported the optical temperature dependence of tin-vacancy (SnV) at low and room temperatures. Compared to the previously reported SiV and GeV color centers, the SnV showed a higher susceptibility. The precision of the SnV thermometer was demonstrated to be as high as $500\ mK/\sqrt{Hz}$ for an ensemble of SnV color centers. Moreover, the linewidth of the SnV was shown to vary linearly with temperatures over a very wide range and can therefore act as independent verification of temperature measurements based on the line position. Then a fiber thermometer probe based on germanium-vacancy (GeV) has been demonstrated. We get temperature resolution better than 20 mK/ Hz capable of producing 2-D 25 μm spatial resolution thermal images.

Those results shows the promising future for group IV color centers in temperature sensing applications. The fact that all three optical thermometers (SiV, GeV, and SnV) have similar sensitivities suggests that many more examples will be discovered in the future, open the door for multiple diamond-based luminescent thermometers for biological applications

For dark exciton in $CsPbX_3$ semiconductor, our results present clear evidence for the readily accessible dark ground exciton state in strongly quantum-confined $CsPbBr_3$ NCs. In contrast to weakly confined NCs, strongly confined QDs, NWs, and NPLs of $CsPbBr_3$ exhibit intense and long-lived dark exciton PL < ~20 K due to the large confinement-enhanced splitting between bright and dark states. In a follow up study, we investigated

size-dependent properties of dark exciton PL in strongly quantum confined $CsPbBr_3$ and $CsPbI_3$ perovskite QDs with focus on the bright–dark splitting energy and dark exciton PL lifetime. A systematic study of the size-dependence showed that both ΔE_{BD} and τ_D increase with increasing quantum confinement. ΔE_{BD} showed approximately linear increase with $1/l^3$ suggesting the dominant role of the enhanced electron–hole exchange energy in determining the magnitude of ΔE_{BD}. The increases in τ_D with increasing quantum confinement, indicative of the decreased dark exciton oscillator strength, may be due to the larger ΔE_{BD} that diminishes the effect of perturbation that gives rise to non-zero oscillator strength by mixing bright and dark states.

Our results clearly show the importance of quantum confinement in determining the nature of the emitting states at cryogenic temperatures and the accessibility of the emitting dark exciton with long lifetime. Those results also stablishes the exciting possibility to take advantage of the superior photonic properties of strongly confined MHPs in the applications utilizing long-lived dark states

APPENDIX A

DATA ANALYSIS FOR GEV THERMOMETRY

A.1 Sample Calculation of Thermometry Accuracy and Resolution

In this section, we give a detailed explanation of thermometry accuracy and resolution. Suppose we get a set of sample data like illustrated in Figure 4.1(a). a_n, b_n, c_n are linewidth measured at that specific time and temperature. As in main text, the thermometry accuracy is defined as $\delta T_{acc} = \delta m_n \langle \langle \lambda_w \rangle_n \rangle_T$. δm_n is the fitting error when we do a linear regression to a set of (λ_w, T), where n is the number of data points we use for each temperature. For example, if we choose data points (a_1, T_a), (b_1, T_b), (c_1, T_c) and do a linear regression. We get the slope equals $k_1 \pm k_1'$, then k_1' is our δm_1. Similarly, if we use (a_1, T_a), (a_2, T_a), (b_1, T_b), (b_2, T_b), (c_1, T_c), (c_2, T_c) and get the slope $k_2 \pm k_2'$. Then this k_2' will be our δm_2. $\langle \lambda_w \rangle_n$ is the average of linewidth over n sample, for example, $\langle \lambda_w \rangle_3$ give us an array of $(\langle a \rangle_3, \langle b \rangle_3, \langle c \rangle_3)$, where $\langle a \rangle_3 = 1/3 \sum_1^3 a_i$ and similarly for $\langle b \rangle_3, \langle c \rangle_3$. Then $\langle \langle \lambda_w \rangle_n \rangle_T$ is the average for all temperature, and in our case $\langle \langle \lambda_w \rangle_3 \rangle_T = 1/3 \, (\langle a \rangle_3 + \langle b \rangle_3 + \langle c \rangle_3)$. So $\langle \langle \lambda_w \rangle_n \rangle_T$ is trying to get an average λ_w over the whole measured temperature range. Then this average linewidth times the error of slope $\frac{\delta T}{\delta \lambda_w}$ give us the error of temperature. This is consistent with the intuition, that the deviation of the measured temperature value is the accuracy of thermometry.

Temperature resolution of our probe is defined as the thermal noise over a given bandwidth. That is the Fourier transform of $m(\lambda_{w,i} - \langle \lambda_w \rangle_{T_i})$. By definition, $\lambda_{w,i} - \langle \lambda_w \rangle_{T_i}$ is mean to remove the linewidth shift from temperature and only left its fluctuation

over time. In the example of our sample data, this is to change data set from $(a_1, a_2, \dots, a_6, b_1, \dots)$ to $(a_1 - \langle a \rangle_6, a_2 - \langle a \rangle_3, \dots, a_6 - \langle a \rangle_3, b_1 - \langle b \rangle_3, \dots)$ as illustrated in Figure 4.1(b). Those modified linewidth times a calibration slope $\frac{\delta T}{\delta \lambda_w}$, in our case k_6, give us the temperature fluctuation over time $(t, \delta T)$. Then Fourier transform of this set of data will give us the temperature fluctuation spectrum $(f, \delta T)$. This will tell us how much temperature fluctuation we should expect when we collect data in that frequency. As shown in main text, our resolution or sensitivity is 20mK if we do 1s integration with 20 to 30mW lase power.

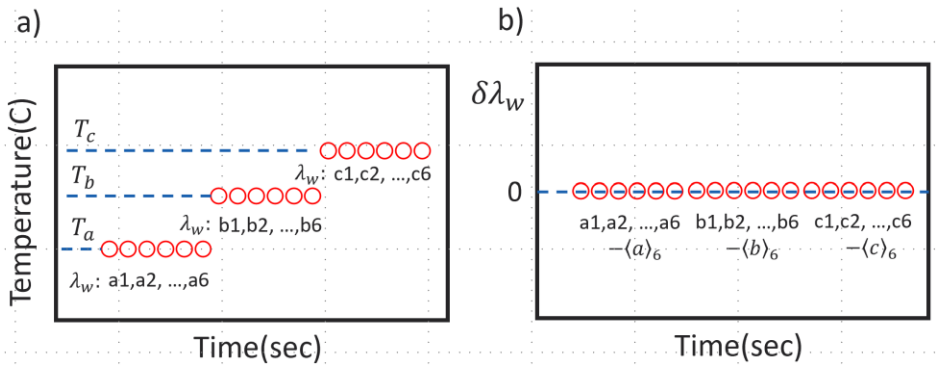

Figure 4.1 (a) Sample data of linewidth with temperature versus time (b) illustration of data set after process of $\lambda_{w,i} - \langle \lambda_w \rangle_{T_i}$

APPENDIX B

EXPERIMENTAL SETUP

B.1 Magnetic Cryostat with Optical Collection for $CsPbX_3$

For the measurement of magnetic field-dependent PL lifetime, the sample film (NCs dispersed in polystyrene matrix) on a sapphire substrate was mounted in a magneto optical cryostat oriented in Faraday geometry equipped with a superconducting magnet providing up to 8 T of magnetic field (Cryogenic Limited). The NC sample was excited with 405nm, 150 ns excitation pulses produced using a CW laser and acousto-optic modulator at the repetition rate of 10-100 kHz that varied depending on the width of the time window of the measurement. The intensity of the excitation light was ~30W/cm^2. Time-resolved photoluminescence was collected by time-correlated single photon counting (Pico Harp 300) with an avalanche photodiode. 150 ns excitation pulse width was sufficient to measure the PL decay dynamics of dark exciton with 1-10s lifetime, while it was too long to reliably measure the fast-decaying PL lifetime in NWs and NPLs that show <50ps decay time. The setup details are illustrated in Figure 4.2

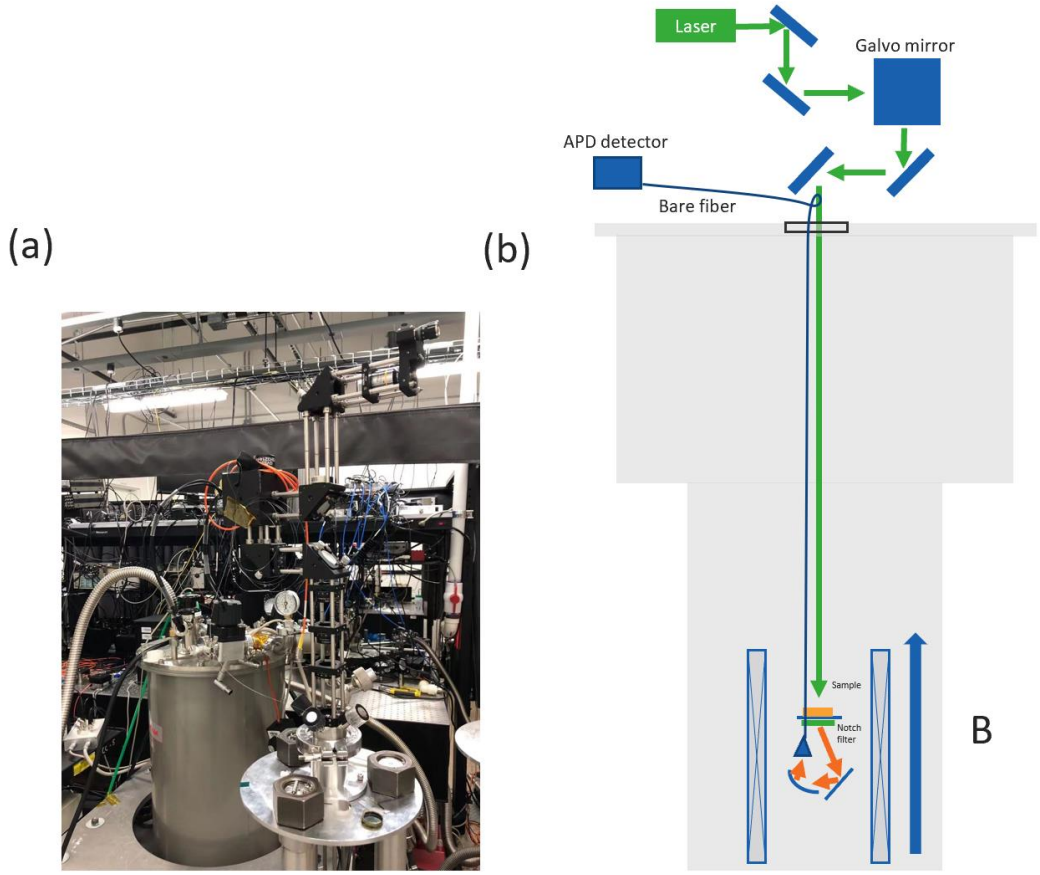

Figure 4.2 (a) Picture of magnetic cryostat with optical insert on side (b) Illustration of measurement optics design

APPENDIX C

MODE FOR DARK EXCITON

C.1 Simple mode for understanding dark exciton properties

There are two key signatures of dark exciton, microsecond long lifetime and lifetime dependency under magnetic field. We use those properties to identify the dark exciton in our main text. Here we will use a simple mode based on Ref[16-18] to explain the origin of these two properties.

Within effective mass model, the valence band of $CsPbX_3$ can be described as combination of Pb 6s and Br 4p atomic orbital with overall s symmetry. So the hole can be described as $|\uparrow\rangle_h = |S\rangle|\uparrow\rangle$ or $|\downarrow\rangle_h = |S\rangle|\downarrow\rangle$. Similarly the conduction band can be described as combination of Pb 6p orbitals $|X\rangle$, $|Y\rangle$ and $|Z\rangle$. The final state of electron is a doubly degenerate state with overall angular momentum $J_e = 1/2$ due to spin-orbit coupling as shown below

$$\begin{aligned} |\Uparrow\rangle_h &= \frac{1}{\sqrt{3}}[(\,|X\rangle + i|Y\rangle)|\downarrow\rangle + \,|Z\rangle|\uparrow\rangle] \\ |\Downarrow\rangle_h &= \frac{1}{\sqrt{3}}[\,|Z\rangle|\downarrow\rangle - (\,|X\rangle - i|Y\rangle)|\uparrow\rangle] \end{aligned} \qquad \text{C. 1 1}$$

Then the exciton level is obtained by combining that of electron and hole. It is four degenerated with states shown below

$$\begin{aligned} |\Psi_{0,0}\rangle &= \frac{1}{\sqrt{2}}[|\Downarrow\rangle_e|\uparrow\rangle_h - |\Uparrow\rangle_e|\downarrow\rangle_h] \\ |\Psi_{1,-1}\rangle &= |\Downarrow\rangle_e|\uparrow\rangle_h \\ |\Psi_{1,0}\rangle &= \frac{1}{\sqrt{2}}[|\Downarrow\rangle_e|\uparrow\rangle_h + |\Uparrow\rangle_e|\downarrow\rangle_h] \\ |\Psi_{1,+1}\rangle &= |\Uparrow\rangle_e|\uparrow\rangle_h \end{aligned} \qquad \text{C. 1 2}$$

$J = 0$ state is forbidden in dipole transition, so it's a dark exciton with very small decay rate. In our case the lifetime is microsecond scale. On the contrary, the $J = 1/2$ state is optical active and thus called bright state.

When there is magnetic field, we can describe the paramagnetic behavior by this simple Hamiltonian

$$H = \mathrm{A}\,\vec{J} \cdot \vec{I} - \vec{\mu}_J \cdot \vec{B} - \vec{\mu}_I \cdot \vec{B} \qquad \text{C.1 3}$$

where J and I represent electron and hole respectively. Under the base of $\left(|\Psi_{0,0}\rangle, |\Psi_{1,0}\rangle, |\Psi_{1,-1}\rangle, |\Psi_{1,+1}\rangle\right)$, we can write Hamiltonian in matrix as

$$\begin{pmatrix} -3/4\,A & -\mu\,B\,\Delta g/2 & 0 & 0 \\ -\mu\,B\,\Delta g/2 & A/4 & 0 & 0 \\ 0 & 0 & A/4 - B\,\Sigma g/2 & 0 \\ 0 & 0 & 0 & A/4 + B\,\Sigma g/2 \end{pmatrix} \qquad \text{C.1 4}$$

where $\Delta g = g_e - g_h$ is the different of g factor for electron and hole, and Σg is their sum, A is the electron hole exchange interaction strength, μ is the Bohr magneton. According to this Hamiltonian, $|\Psi_{1,-1}\rangle$ and $|\Psi_{1,+1}\rangle$ will undergo normal Zeeman effect while states $|\Psi_{0,0}\rangle$ and $|\Psi_{1,0}\rangle$ will mix under magnetic field. This mix will result in two effects. First the energy level of $|\Psi_{0,0}\rangle$ and $|\Psi_{1,0}\rangle$ will start to shift under magnetic field. This is consistent with the research work on $FAPbBr_3$ done by Tamarat, Bodnarchuk et al.[17] Second is that the lifetime of dark exciton will become shorter with higher magnetic field. The new wave functions after mixing will be $|\widetilde{\Psi}_{i,0}\rangle = b_{i0}|\Psi_{0,0}\rangle + b_{i1}|\Psi_{1,0}\rangle$ $(i = 0,1)$. So with higher magnetic field, dark exciton $|\Psi_{0,0}\rangle$ will gain more oscillation strength while bright exciton $|\Psi_{1,0}\rangle$ will lose more oscillation strength. This is consistent with what we see in chapter 4, the lifetime of long component is shorter with larger magnetic field.

C.2 Estimation of τ_B and τ_{BD} from the Steady State PL Spectra

At 5 K, the fast-decay dynamics represent the sum of the relaxation of the bright exciton and transfer from bright to dark exciton level if dark exciton relaxation is sufficiently slow compared to all other processes

$$1/\tau_B + 1/\tau_{BD} = 1/\tau_{fast} \qquad \text{C. 2 1}$$

Because $\Delta E_{BD} >> kT$ at 5K, thermal excitation from bright to dark state can be ignored. We can take the ratio of the PL intensities from bright (I_B) and dark (I_D) exciton in steady state PL spectra at 5K as the branching ratio for bright exciton relaxation and bright-to-dark transition under the following two assumptions: (i) The time scale for cooling from the initially excited level to the bandedge bright exciton level is much shorter than τ_B and τ_{BD}, (ii) nonradiative decay of bright and dark exciton is not significant at 5 K

$$\frac{\tau_B}{\tau_{BD}} = \frac{I_D}{I_B} \qquad \text{C. 2 2}$$

Assumption (i) is reasonable since the time scale for cooling of hot exciton reported is typically sub ps in perovskite nanocrystals. Assumption (ii) is less straightforward, but we assume it is approximately valid considering the near-maximum PL intensity at 5 K as shown in Figure 4.3. Since the bright and dark excitons PL are spectrally well separated, we can obtain $\frac{I_D}{I_B}$ accurately from the fitting of the steady state PL shown in Figure 3.2. For the NPL sample, $\frac{I_D}{I_B} = 2.3$, therefore $\tau_B = 2.3\,\tau_{BD}$. Also from experimental data $1/\tau_B + 1/\tau_{BD} = 1/\tau_{fast} = 1/38\,ps$, then from the two equations above, we obtain $\tau_{BD} = 54\,ps$ and $\tau_B = 124\,ps$

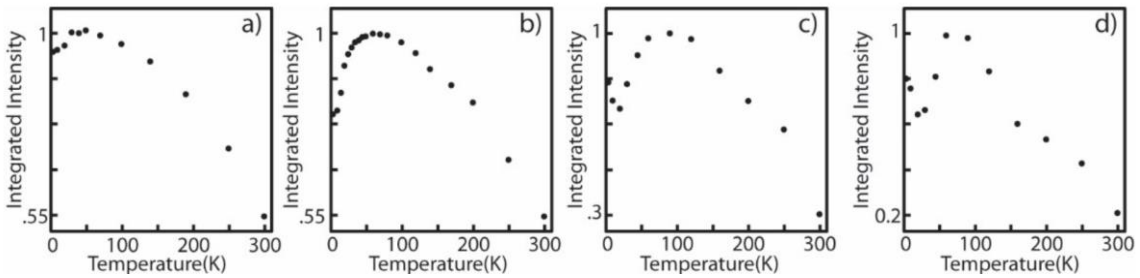

Figure 4.3* Normalized temperature dependent integrated intensities from the weekly confined NC, and strongly confined QD, NW, and NPL films used in the main text(a-d)

Sample calculation of τ_B and τ_{BD} for NPLs:

Since the bright and dark excitons PL are spectrally well separated, we can obtain $\frac{I_D}{I_B}$ accurately from the fitting of the steady state PL shown in Figure 3.2. For the NPL sample, $\frac{I_D}{I_B} = 2.3$, therefore $\tau_B = 2.3\,\tau_{BD}$. Also from experimental data $1/\tau_B + 1/\tau_{BD} = 1/\tau_{fast} = 1/38\ ps$, then from the two equations above, we obtain $\tau_{BD} = 54\ ps$ and $\tau_B = 124\ ps$

*Reprinted from Rossi, Liu et al. 2020

C.3 Three-Level Kinetic Model and Temperature-Dependent τ_{fast} and τ_{slow}

It is common to model the kinetics of the bright and dark exciton after a three-level system with two emitting states (bright and dark) with lifetime τ_B and τ_D separated in energy by ΔE_{BD}. Transition between these two states occurs via absorption or emission of a phonon with rates$\gamma_{DB} = \gamma_0 N_B$, and $\gamma_{BD} = \gamma_0(N_B + 1)$, where γ_0 is the zero-temperature bright-to-dark transition rate and N_B is the phonon occupation number. We can model the time dependent population dynamics of the bright (P_B) and dark (P_D) state as follows

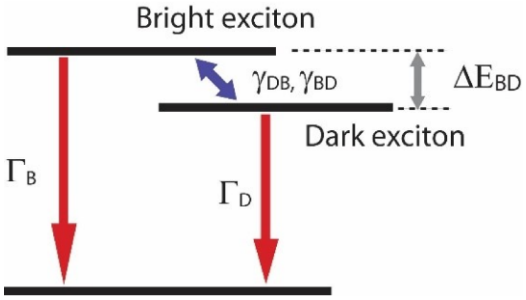

$$\frac{dP_B}{dt} = -\big(\Gamma_B + \gamma_0(N_B + 1)\big)P_B + \gamma_0 N_B P_D \qquad \text{C.3 1}$$

$$\frac{dP_D}{dt} = -(\Gamma_D + \gamma_0 N_B)P_D + \gamma_0(N_B + 1)P_B \qquad \text{C.3 2}$$

Where $\Gamma_B = \frac{1}{\tau_B}$, $\Gamma_D = \frac{1}{\tau_D}$, $\gamma_0(N_B + 1) = \frac{1}{\tau_{BD}}$, $\gamma_0 N_B = \frac{1}{\tau_{DB}}$, and $N_B = \frac{1}{(\exp(\Delta E_{BD}/kT) - 1)}$ at temperature T.

Solving these differential equations with $P_B(t = 0) = 1$, $P_D(t = 0) = 0$, we get the biexponential decay for both $P_B(t)$ and $P_D(t)$ with the two temperature-dependent rate constants $\Gamma_{slow}(T) = 1/\tau_{slow}(T)$ and $\Gamma_{fast}(T) = 1/\tau_{fast}(T)$ expressed as follows.

$\Gamma_{(\text{fast}(+),\text{slow}(-))}(T)$

$$= \frac{1}{2}(\Gamma_B + \Gamma_D + \gamma_0 + 2\mathrm{N}_B\gamma_0$$

$$\pm \sqrt{(\Gamma_B - \Gamma_D + \gamma_0)^2 + 4\mathrm{N}_B{\gamma_0}^2(\mathrm{N}_B + 1)} \qquad \text{C. 3 3}$$

At 5 K, $N_B \approx 0$. Under the condition $\Gamma_D \ll \Gamma_B$ and γ_0, we obtained the following two equations.

$$\Gamma_{slow}(5K) \approx \frac{1}{2}\left(\Gamma_B + \Gamma_D + \gamma_0 - \sqrt{(\Gamma_B - \Gamma_D + \gamma_0)^2}\right) = \Gamma_D = \frac{1}{\tau_D} \qquad \text{C. 3 4}$$

$$\Gamma_{fast}(5K) \approx \frac{1}{2}\left(\Gamma_B + \Gamma_D + \gamma_0 + \sqrt{(\Gamma_B - \Gamma_D + \gamma_0)^2}\right) = \Gamma_B + \gamma_0 = \frac{1}{\tau_B} + \frac{1}{\tau_{BD}} \qquad \text{C. 3 5}$$

Therefore, Γ_D, Γ_B and γ_0 can be experimentally determined from PL decay kinetics at 5 K and $\Gamma_{slow}(T)$ and $\Gamma_{fast}(T)$ can be obtained from equations using these parameters. Figure 4.4 (a-c) shows the comparison of the experimental PL decay dynamics at 5 K and the calculated time-dependent PL intensity, I(t), at 5K obtained using equations C.3 1, C.3 2, C.3 6. The time dependent bright and dark exciton populations are converted to the time dependent PL intensity, I(t), using equation C.3 6 where the calculated PL decay kinetics is convoluted with the instrument response function (IRF):

$$I(t) = IRF \otimes \Phi_B\Gamma_B P_B(\mathrm{t}) + \Phi_D\Gamma_D P_D(\mathrm{t}) \qquad \text{C. 3 6}$$

Φ_B and Φ_D are the bright and dark exciton quantum yield (assumed to be the same). Figure 4.4(d-f) shows the comparison of the result from equation C.3 3 with the experimentally measured temperature dependent τ_{slow} and τ_{fast} for strongly confined QDs, NWs and NPLs as nonadjustable parameters. The model fits the experimental data for QDs well. On the other hand, the model overestimates τ_{fast} of NWs and NPLs, suggesting

the presence of an additional thermally activated decay pathway of bright exciton consistent with the more complicated change in relative PL QY for the NWs and NPLs as shown in Figure 4.4.

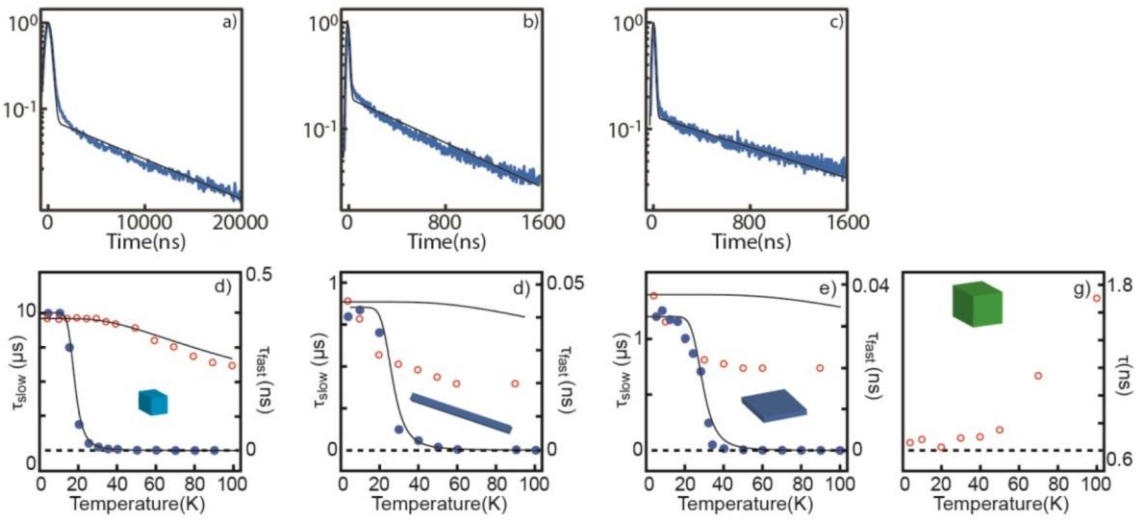

Figure 4.4* (a-c) Comparison of the experimental (blue) and calculated (black) time-dependent PL intensity using equations C.3 4 and C.3 5 for QDs (a), NWs (b) and NPLs (c) at 5K. (d-f) Temperature dependent τ_{fast} (○) and τ_{slow} (●) together with calculated values (solid line) from the model using the equation C.3 3 (g) Nearly single exponential decay time of the PL from weakly confined NCs is shown for comparison.

*Reprinted from Rossi, Liu et al. 2020

REFERENCE

1 Kucsko, G. *et al.* Nanometre-scale thermometry in a living cell. *Nature* **500**, 54-58, doi:10.1038/nature12373 (2013).

2 Kalb, N. *et al.* Entanglement distillation between solid-state quantum network nodes. *Science* **356**, 928-932, doi:10.1126/science.aan0070 (2017).

3 Bradley, C. E. *et al.* A Ten-Qubit Solid-State Spin Register with Quantum Memory up to One Minute. *Physical Review X* **9**, 031045, doi:10.1103/PhysRevX.9.031045 (2019).

4 Balasubramanian, G. *et al.* Ultralong spin coherence time in isotopically engineered diamond. *Nature Materials* **8**, 383-387, doi:10.1038/nmat2420 (2009).

5 Maze, J. R. *et al.* Nanoscale magnetic sensing with an individual electronic spin in diamond. *Nature* **455**, 644-647, doi:10.1038/nature07279 (2008).

6 Siyushev, P. *et al.* Optically Controlled Switching of the Charge State of a Single Nitrogen-Vacancy Center in Diamond at Cryogenic Temperatures. *Physical Review Letters* **110**, 167402, doi:10.1103/PhysRevLett.110.167402 (2013).

7 Bradac, C., Gao, W., Forneris, J., Trusheim, M. E. & Aharonovich, I. Quantum nanophotonics with group IV defects in diamond. *Nature Communications* **10**, 5625, doi:10.1038/s41467-019-13332-w (2019).

8 Sipahigil, A. *et al.* Indistinguishable Photons from Separated Silicon-Vacancy Centers in Diamond. *Physical Review Letters* **113**, 113602, doi:10.1103/PhysRevLett.113.113602 (2014).

9 Sohn, Y.-I. *et al.* Controlling the coherence of a diamond spin qubit through its strain environment. *Nature Communications* **9**, 2012, doi:10.1038/s41467-018-04340-3 (2018).

10 Trusheim, M. E. *et al.* Transform-Limited Photons From a Coherent Tin-Vacancy Spin in Diamond. *Physical Review Letters* **124**, 023602, doi:10.1103/PhysRevLett.124.023602 (2020).

11 Sukachev, D. D. *et al.* Silicon-Vacancy Spin Qubit in Diamond: A Quantum Memory Exceeding 10 ms with Single-Shot State Readout. *Physical Review Letters* **119**, 223602, doi:10.1103/PhysRevLett.119.223602 (2017).

12 Gaebel, T. *et al.* Stable single-photon source in the near infrared. *New Journal of Physics* **6**, 98-98, doi:10.1088/1367-2630/6/1/098 (2004).

13 Yakunin, S. *et al.* Low-threshold amplified spontaneous emission and lasing from colloidal nanocrystals of caesium lead halide perovskites. *Nature Communications* **6**, 8056, doi:10.1038/ncomms9056 (2015).

14 Tan, Z.-K. *et al.* Bright light-emitting diodes based on organometal halide perovskite. *Nature Nanotechnology* **9**, 687-692, doi:10.1038/nnano.2014.149 (2014).

15 Kim, H.-S. *et al.* Lead Iodide Perovskite Sensitized All-Solid-State Submicron Thin Film Mesoscopic Solar Cell with Efficiency Exceeding 9%. *Scientific Reports* **2**, 591, doi:10.1038/srep00591 (2012).

16 Becker, M. A. *et al.* Bright triplet excitons in caesium lead halide perovskites. *Nature* **553**, 189-193, doi:10.1038/nature25147 (2018).

17 Tamarat, P. *et al.* The ground exciton state of formamidinium lead bromide perovskite nanocrystals is a singlet dark state. *Nature Materials* **18**, 717-724, doi:10.1038/s41563-019-0364-x (2019).

18 Yu, Z. G. Effective-mass model and magneto-optical properties in hybrid perovskites. *Scientific Reports* **6**, 28576, doi:10.1038/srep28576 (2016).

19 Brovelli, S. *et al.* Nano-engineered electron–hole exchange interaction controls exciton dynamics in core–shell semiconductor nanocrystals. *Nature Communications* **2**, 280, doi:10.1038/ncomms1281 (2011).

20 Clark, D. G., Brinkman, M. & Neville, S. D. Microcalorimetric measurements of heat production in brown adipocytes from control and cafeteria-fed rats. *Biochemical Journal* **235**, 337-342, doi:10.1042/bj2350337 (1986).

21 Lowell, B. B. & Spiegelman, B. M. Towards a molecular understanding of adaptive thermogenesis. *Nature* **404**, 652-660, doi:10.1038/35007527 (2000).

22 Michalet, X. *et al.* Quantum Dots for Live Cells, in Vivo Imaging, and Diagnostics. *Science* **307**, 538-544, doi:10.1126/science.1104274 (2005).

23 Maestro, L. M. *et al.* CdSe Quantum Dots for Two-Photon Fluorescence Thermal Imaging. *Nano Letters* **10**, 5109-5115, doi:10.1021/nl1036098 (2010).

24 Yang, J.-M., Yang, H. & Lin, L. Quantum Dot Nano Thermometers Reveal Heterogeneous Local Thermogenesis in Living Cells. *ACS Nano* **5**, 5067-5071, doi:10.1021/nn201142f (2011).

25 Walling, M. A., Novak, J. A. & Shepard, J. R. E. Quantum Dots for Live Cell and In Vivo Imaging. *International Journal of Molecular Sciences* **10**, doi:10.3390/ijms10020441 (2009).

26 Koide, Y. *et al.* Development of NIR Fluorescent Dyes Based on Si–rhodamine for in Vivo Imaging. *Journal of the American Chemical Society* **134**, 5029-5031, doi:10.1021/ja210375e (2012).

27 Kiyonaka, S. *et al.* Genetically encoded fluorescent thermosensors visualize subcellular thermoregulation in living cells. *Nature Methods* **10**, 1232-1238, doi:10.1038/nmeth.2690 (2013).

28 Yu, J. *et al.* Near-infrared fluorescence imaging using organic dye nanoparticles. *Biomaterials* **35**, 3356-3364, doi:https://doi.org/10.1016/j.biomaterials.2014.01.004 (2014).

29 Donner, J. S., Thompson, S. A., Kreuzer, M. P., Baffou, G. & Quidant, R. Mapping Intracellular Temperature Using Green Fluorescent Protein. *Nano Letters* **12**, 2107-2111, doi:10.1021/nl300389y (2012).

30 Zheng, X. *et al.* High-Contrast Visualization of Upconversion Luminescence in Mice Using Time-Gating Approach. *Analytical Chemistry* **88**, 3449-3454, doi:10.1021/acs.analchem.5b04626 (2016).

31 Okabe, K. *et al.* Intracellular temperature mapping with a fluorescent polymeric thermometer and fluorescence lifetime imaging microscopy. *Nature Communications* **3**, 705, doi:10.1038/ncomms1714 (2012).

32 Zohar, O. *et al.* Thermal Imaging of Receptor-Activated Heat Production in Single Cells. *Biophysical Journal* **74**, 82-89, doi:https://doi.org/10.1016/S0006-3495(98)77769-0 (1998).

33 Vetrone, F. *et al.* Temperature Sensing Using Fluorescent Nanothermometers. *ACS Nano* **4**, 3254-3258, doi:10.1021/nn100244a (2010).

34 Zhang, Q. *et al.* Gold nanoparticles as a contrast agent forin vivotumor imaging with photoacoustic tomography. *Nanotechnology* **20**, 395102, doi:10.1088/0957-4484/20/39/395102 (2009).

35 Resch-Genger, U., Grabolle, M., Cavaliere-Jaricot, S., Nitschke, R. & Nann, T. Quantum dots versus organic dyes as fluorescent labels. *Nature Methods* **5**, 763-775, doi:10.1038/nmeth.1248 (2008).

36 Alkahtani, M. H., Gomes, C. L. & Hemmer, P. R. Engineering water-tolerant core/shell upconversion nanoparticles for optical temperature sensing. *Opt. Lett.* **42**, 2451-2454, doi:10.1364/OL.42.002451 (2017).

37 Zhu, X. *et al.* Temperature-feedback upconversion nanocomposite for accurate photothermal therapy at facile temperature. *Nature Communications* **7**, 10437, doi:10.1038/ncomms10437 (2016).

38 Jiang, G. *et al.* 794 nm excited core–shell upconversion nanoparticles for optical temperature sensing. *RSC Advances* **6**, 11795-11801, doi:10.1039/C5RA27203C (2016).

39 Alkahtani, M., Jiang, L., Brick, R., Hemmer, P. & Scully, M. Nanometer-scale luminescent thermometry in bovine embryos. *Opt. Lett.* **42**, 4812-4815, doi:10.1364/OL.42.004812 (2017).

40 Boyer, J.-C. & van Veggel, F. C. J. M. Absolute quantum yield measurements of colloidal NaYF4: Er3+, Yb3+ upconverting nanoparticles. *Nanoscale* **2**, 1417-1419, doi:10.1039/C0NR00253D (2010).

41 McGuinness, L. P. *et al.* Quantum measurement and orientation tracking of fluorescent nanodiamonds inside living cells. *Nature Nanotechnology* **6**, 358-363, doi:10.1038/nnano.2011.64 (2011).

42 Chang, Y.-R. *et al.* Mass production and dynamic imaging of fluorescent nanodiamonds. *Nature Nanotechnology* **3**, 284-288, doi:10.1038/nnano.2008.99 (2008).

43 Fu, C.-C. *et al.* Characterization and application of single fluorescent nanodiamonds as cellular biomarkers. *Proceedings of the National Academy of Sciences* **104**, 727, doi:10.1073/pnas.0605409104 (2007).

44 Gruber, A. *et al.* Scanning Confocal Optical Microscopy and Magnetic Resonance on Single Defect Centers. *Science* **276**, 2012-2014, doi:10.1126/science.276.5321.2012 (1997).

45 Schrand, A. M. *et al.* Are Diamond Nanoparticles Cytotoxic? *The Journal of Physical Chemistry B* **111**, 2-7, doi:10.1021/jp066387v (2007).

46 Acosta, V. M. *et al.* Temperature Dependence of the Nitrogen-Vacancy Magnetic Resonance in Diamond. *Physical Review Letters* **104**, 070801, doi:10.1103/PhysRevLett.104.070801 (2010).

47 Wang, J. *et al.* High-sensitivity temperature sensing using an implanted single nitrogen-vacancy center array in diamond. *Physical Review B* **91**, 155404, doi:10.1103/PhysRevB.91.155404 (2015).

48 Jakobi, I. *et al.* Measuring broadband magnetic fields on the nanoscale using a hybrid quantum register. *Nature Nanotechnology* **12**, 67-72, doi:10.1038/nnano.2016.163 (2017).

49 Barry, J. F. *et al.* Optical magnetic detection of single-neuron action potentials using quantum defects in diamond. *Proceedings of the National Academy of Sciences* **113**, 14133, doi:10.1073/pnas.1601513113 (2016).

50 Gao, R. *et al.* A large-scale screen reveals genes that mediate electrotaxis in Dictyostelium discoideum. *Science Signaling* **8**, ra50-ra50, doi:10.1126/scisignal.aab0562 (2015).

51 Dolde, F. *et al.* Electric-field sensing using single diamond spins. *Nature Physics* **7**, 459-463, doi:10.1038/nphys1969 (2011).

52 Tsai, P.-C. *et al.* Measuring Nanoscale Thermostability of Cell Membranes with Single Gold–Diamond Nanohybrids. *Angewandte Chemie International Edition* **56**, 3025-3030, doi:https://doi.org/10.1002/anie.201700357 (2017).

53 Plakhotnik, T., Aman, H. & Chang, H.-C. All-optical single-nanoparticle ratiometric thermometry with a noise floor of 0.3 K Hz−1/2. *Nanotechnology* **26**, 245501, doi:10.1088/0957-4484/26/24/245501 (2015).

54 Plakhotnik, T. & Gruber, D. Luminescence of nitrogen-vacancy centers in nanodiamonds at temperatures between 300 and 700 K: perspectives on nanothermometry. *Physical Chemistry Chemical Physics* **12**, 9751-9756, doi:10.1039/C001132K (2010).

55 Nguyen, C. T. *et al.* All-optical nanoscale thermometry with silicon-vacancy centers in diamond. *Applied Physics Letters* **112**, 203102, doi:10.1063/1.5029904 (2018).

56 Fan, J.-W. *et al.* Germanium-Vacancy Color Center in Diamond as a Temperature Sensor. *ACS Photonics* **5**, 765-770, doi:10.1021/acsphotonics.7b01465 (2018).

57 Iwasaki, T. *et al.* Tin-Vacancy Quantum Emitters in Diamond. *Physical Review Letters* **119**, 253601, doi:10.1103/PhysRevLett.119.253601 (2017).

58 Palyanov, Y. N., Kupriyanov, I. N., Borzdov, Y. M. & Surovtsev, N. V. Germanium: a new catalyst for diamond synthesis and a new optically active impurity in diamond. *Scientific Reports* **5**, 14789, doi:10.1038/srep14789 (2015).

59 Palyanov, Y. N., Kupriyanov, I. N., Borzdov, Y. M., Khokhryakov, A. F. & Surovtsev, N. V. High-Pressure Synthesis and Characterization of Ge-Doped Single Crystal Diamond. *Crystal Growth & Design* **16**, 3510-3518, doi:10.1021/acs.cgd.6b00481 (2016).

60 Sovyk, D. N. *et al.* Growth of CVD diamond nanopillars with imbedded silicon-vacancy color centers. *Optical Materials* **61**, 25-29, doi:https://doi.org/10.1016/j.optmat.2016.08.002 (2016).

61 Sovyk, D. *et al.* Fabrication of diamond microstub photoemitters with strong photoluminescence of SiV color centers: bottom-up approach. *Applied Physics A* **118**, 17-21, doi:10.1007/s00339-014-8877-2 (2015).

62 Häußler, S. *et al.* Photoluminescence excitation spectroscopy of SiV−and GeV−color center in diamond. *New Journal of Physics* **19**, 063036, doi:10.1088/1367-2630/aa73e5 (2017).

63 Iwasaki, T. *et al.* Germanium-Vacancy Single Color Centers in Diamond. *Scientific Reports* **5**, 12882, doi:10.1038/srep12882 (2015).

64 Bhaskar, M. K. *et al.* Quantum Nonlinear Optics with a Germanium-Vacancy Color Center in a Nanoscale Diamond Waveguide. *Physical Review Letters* **118**, 223603, doi:10.1103/PhysRevLett.118.223603 (2017).

65 Jahnke, K. D. *et al.* Electron–phonon processes of the silicon-vacancy centre in diamond. *New Journal of Physics* **17**, 043011, doi:10.1088/1367-2630/17/4/043011 (2015).

66 Tanimoto, R. *et al.* Detection of Temperature Difference in Neuronal Cells. *Scientific Reports* **6**, 22071, doi:10.1038/srep22071 (2016).

67 Sarua, A. *et al.* Integrated micro-Raman/infrared thermography probe for monitoring of self-heating in AlGaN/GaN transistor structures. *IEEE Transactions on Electron Devices* **53**, 2438-2447, doi:10.1109/TED.2006.882274 (2006).

68 Mital, M. & Scott, E. P. Thermal detection of embedded tumors using infrared imaging. *J Biomech Eng* **129**, 33-39, doi:10.1115/1.2401181 (2007).

69 Gorbach, A. M., Heiss, J. D., Kopylev, L. & Oldfield, E. H. Intraoperative infrared imaging of brain tumors. *J Neurosurg* **101**, 960-969, doi:10.3171/jns.2004.101.6.0960 (2004).

70 Aharonovich, I., Englund, D. & Toth, M. Solid-state single-photon emitters. *Nature Photonics* **10**, 631-641, doi:10.1038/nphoton.2016.186 (2016).

71 Aharonovich, I., Greentree, A. D. & Prawer, S. Diamond photonics. *Nature Photonics* **5**, 397-405, doi:10.1038/nphoton.2011.54 (2011).

72 Siyushev, P. *et al.* Optical and microwave control of germanium-vacancy center spins in diamond. *Physical Review B* **96**, 081201, doi:10.1103/PhysRevB.96.081201 (2017).

73 Ekimov, E. A. *et al.* Germaniu• vacancy color center in isotopically enriched diamonds synthesized at high pressures. *JETP Letters* **102**, 701-706 (2015).

74 Alkahtani, M. *et al.* Tin-vacancy in diamonds for luminescent thermometry. *Applied Physics Letters* **112**, 241902, doi:10.1063/1.5037053 (2018).

75 Fedotov, I. V. *et al.* Fiber-based thermometry using optically detected magnetic resonance. *Applied Physics Letters* **105**, 261109, doi:10.1063/1.4904798 (2014).

76 Wadsworth, W. J. *et al.* Very high numerical aperture fibers. *IEEE Photonics Technology Letters* **16**, 843-845, doi:10.1109/LPT.2004.823689 (2004).

77 Song, J. *et al.* Quantum Dot Light-Emitting Diodes Based on Inorganic Perovskite Cesium Lead Halides (CsPbX3). *Advanced Materials* **27**, 7162-7167, doi:https://doi.org/10.1002/adma.201502567 (2015).

78 Wang, Y. *et al.* All-Inorganic Colloidal Perovskite Quantum Dots: A New Class of Lasing Materials with Favorable Characteristics. *Advanced Materials* **27**, 7101-7108, doi:https://doi.org/10.1002/adma.201503573 (2015).

79 Koscher, B. A., Swabeck, J. K., Bronstein, N. D. & Alivisatos, A. P. Essentially Trap-Free CsPbBr3 Colloidal Nanocrystals by Postsynthetic Thiocyanate Surface Treatment. *Journal of the American Chemical Society* **139**, 6566-6569, doi:10.1021/jacs.7b02817 (2017).

80 Protesescu, L. *et al.* Nanocrystals of Cesium Lead Halide Perovskites (CsPbX3, X = Cl, Br, and I): Novel Optoelectronic Materials Showing Bright Emission with Wide Color Gamut. *Nano Letters* **15**, 3692-3696, doi:10.1021/nl5048779 (2015).

81 Yan, F. & Demir, H. V. LEDs using halide perovskite nanocrystal emitters. *Nanoscale* **11**, 11402-11412, doi:10.1039/C9NR03533H (2019).

82 Utzat, H. *et al.* Coherent single-photon emission from colloidal lead halide perovskite quantum dots. *Science* **363**, 1068-1072, doi:10.1126/science.aau7392 (2019).

83 Akkerman, Q. A. *et al.* Tuning the Optical Properties of Cesium Lead Halide Perovskite Nanocrystals by Anion Exchange Reactions. *Journal of the American Chemical Society* **137**, 10276-10281, doi:10.1021/jacs.5b05602 (2015).

84 Dong, Y. *et al.* Precise Control of Quantum Confinement in Cesium Lead Halide Perovskite Quantum Dots via Thermodynamic Equilibrium. *Nano Letters* **18**, 3716-3722, doi:10.1021/acs.nanolett.8b00861 (2018).

85 Zhou, G., Su, B., Huang, J., Zhang, Q. & Xia, Z. Broad-band emission in metal halide perovskites: Mechanism, materials, and applications. *Materials Science and Engineering: R: Reports* **141**, 100548, doi:https://doi.org/10.1016/j.mser.2020.100548 (2020).

86 Lao, X. *et al.* Luminescence and thermal behaviors of free and trapped excitons in cesium lead halide perovskite nanosheets. *Nanoscale* **10**, 9949-9956, doi:10.1039/C8NR01109E (2018).

87 Parobek, D. *et al.* Exciton-to-Dopant Energy Transfer in Mn-Doped Cesium Lead Halide Perovskite Nanocrystals. *Nano Letters* **16**, 7376-7380, doi:10.1021/acs.nanolett.6b02772 (2016).

88 Schaller, R. D. *et al.* Revealing the Exciton Fine Structure of PbSe Nanocrystal Quantum Dots Using Optical Spectroscopy in High Magnetic Fields. *Physical Review Letters* **105**, 067403, doi:10.1103/PhysRevLett.105.067403 (2010).

89 Li, Z. *et al.* Emerging photoluminescence from the dark-exciton phonon replica in monolayer WSe2. *Nature Communications* **10**, 2469, doi:10.1038/s41467-019-10477-6 (2019).

90 Nirmal, M. *et al.* Observation of the "Dark Exciton" in CdSe Quantum Dots. *Physical Review Letters* **75**, 3728-3731, doi:10.1103/PhysRevLett.75.3728 (1995).

91 Xu, K., Vliem, J. F. & Meijerink, A. Long-Lived Dark Exciton Emission in Mn-Doped CsPbCl3 Perovskite Nanocrystals. *The Journal of Physical Chemistry C* **123**, 979-984, doi:10.1021/acs.jpcc.8b12035 (2019).

92 Sercel, P. C. *et al.* Exciton Fine Structure in Perovskite Nanocrystals. *Nano Letters* **19**, 4068-4077, doi:10.1021/acs.nanolett.9b01467 (2019).

93 Nirmal, M. *et al.* Observation of the "Dark exciton" in CdSe quantum dots. *Phys Rev Lett* **75**, 3728-3731, doi:10.1103/PhysRevLett.75.3728 (1995).

94 Kuno, M., Lee, J.-K., Dabbousi, B. O., Mikulec, F. V. & Bawendi, M. G. The band edge luminescence of surface modified CdSe nanocrystallites: Probing the luminescing state. *The Journal of Chemical Physics* **106**, 9869-9882 (1997).

95 Biadala, L. *et al.* Recombination Dynamics of Band Edge Excitons in Quasi-Two-Dimensional CdSe Nanoplatelets. *Nano Letters* **14**, 1134-1139, doi:10.1021/nl403311n (2014).

96 Crooker, S. A., Barrick, T., Hollingsworth, J. A. & Klimov, V. I. Multiple temperature regimes of radiative decay in CdSe nanocrystal quantum dots: Intrinsic limits to the dark-exciton lifetime. *Applied Physics Letters* **82**, 2793-2795, doi:10.1063/1.1570923 (2003).

97 de Mello Donegá, C., Bode, M. & Meijerink, A. Size- and temperature-dependence of exciton lifetimes in CdSe quantum dots. *Physical Review B* **74**, 085320, doi:10.1103/PhysRevB.74.085320 (2006).

98 Dong, Y. *et al.* Controlling Anisotropy of Quantum-Confined CsPbBr3 Nanocrystals by Combined Use of Equilibrium and Kinetic Anisotropy. *Chemistry of Materials* **31**, 5655-5662, doi:10.1021/acs.chemmater.9b01515 (2019).

99 Rainò, G. *et al.* Single Cesium Lead Halide Perovskite Nanocrystals at Low Temperature: Fast Single-Photon Emission, Reduced Blinking, and Exciton Fine Structure. *ACS Nano* **10**, 2485-2490, doi:10.1021/acsnano.5b07328 (2016).

100 Canneson, D. *et al.* Negatively Charged and Dark Excitons in CsPbBr3 Perovskite Nanocrystals Revealed by High Magnetic Fields. *Nano Letters* **17**, 6177-6183, doi:10.1021/acs.nanolett.7b02827 (2017).

101 Chen, L. *et al.* Composition-Dependent Energy Splitting between Bright and Dark Excitons in Lead Halide Perovskite Nanocrystals. *Nano Letters* **18**, 2074-2080, doi:10.1021/acs.nanolett.8b00184 (2018).

102 Ramade, J. *et al.* Fine structure of excitons and electron–hole exchange energy in polymorphic CsPbBr3 single nanocrystals. *Nanoscale* **10**, 6393-6401, doi:10.1039/C7NR09334A (2018).

103 Tessier, M. D., Javaux, C., Maksimovic, I., Loriette, V. & Dubertret, B. Spectroscopy of Single CdSe Nanoplatelets. *ACS Nano* **6**, 6751-6758, doi:10.1021/nn3014855 (2012).

104 Fu, M. *et al.* Unraveling exciton–phonon coupling in individual FAPbI3 nanocrystals emitting near-infrared single photons. *Nature Communications* **9**, 3318, doi:10.1038/s41467-018-05876-0 (2018).

105 Wu, X. *et al.* Trap States in Lead Iodide Perovskites. *Journal of the American Chemical Society* **137**, 2089-2096, doi:10.1021/ja512833n (2015).

106 Iaru, C. M., Geuchies, J. J., Koenraad, P. M., Vanmaekelbergh, D. & Silov, A. Y. Strong Carrier–Phonon Coupling in Lead Halide Perovskite Nanocrystals. *ACS Nano* **11**, 11024-11030, doi:10.1021/acsnano.7b05033 (2017).

107 Ma, X. *et al.* Mechanism of Single-Photon Upconversion Photoluminescence in All-Inorganic Perovskite Nanocrystals: The Role of Self-Trapped Excitons. *The Journal of Physical Chemistry Letters* **10**, 5989-5996, doi:10.1021/acs.jpclett.9b02289 (2019).

108 Fu, M. *et al.* Neutral and Charged Exciton Fine Structure in Single Lead Halide Perovskite Nanocrystals Revealed by Magneto-optical Spectroscopy. *Nano Letters* **17**, 2895-2901, doi:10.1021/acs.nanolett.7b00064 (2017).

109 Shornikova, E. V. *et al.* Negatively Charged Excitons in CdSe Nanoplatelets. *Nano Letters* **20**, 1370-1377, doi:10.1021/acs.nanolett.9b04907 (2020).

110 Diroll, B. T. *et al.* Semiconductor Nanoplatelet Excimers. *Nano Letters* **18**, 6948-6953, doi:10.1021/acs.nanolett.8b02865 (2018).

111 Labeau, O., Tamarat, P. & Lounis, B. Temperature Dependence of the Luminescence Lifetime of Single $\mathrm{C}\mathrm{d}\mathrm{S}\mathrm{e}/\mathrm{Z}\mathrm{n}\mathrm{S}$ Quantum Dots. *Physical Review Letters* **90**, 257404, doi:10.1103/PhysRevLett.90.257404 (2003).

112 Louyer, Y., Biadala, L., Tamarat, P. & Lounis, B. Spectroscopy of neutral and charged exciton states in single CdSe/ZnS nanocrystals. *Applied Physics Letters* **96**, 203111, doi:10.1063/1.3435464 (2010).

113 Rodina, A. & Efros, A. L. Magnetic Properties of Nonmagnetic Nanostructures: Dangling Bond Magnetic Polaron in CdSe Nanocrystals. *Nano Letters* **15**, 4214-4222, doi:10.1021/acs.nanolett.5b01566 (2015).

114 Meulenberg, R. W. *et al.* Evidence for Ligand-Induced Paramagnetism in CdSe Quantum Dots. *Journal of the American Chemical Society* **131**, 6888-6889, doi:10.1021/ja8098454 (2009).

115 Califano, M., Franceschetti, A. & Zunger, A. Lifetime and polarization of the radiative decay of excitons, biexcitons, and trions in CdSe nanocrystal quantum dots. *Physical Review B* **75**, 115401, doi:10.1103/PhysRevB.75.115401 (2007).

116 Nirmal, M., Murray, C. B. & Bawendi, M. G. Fluorescence-line narrowing in CdSe quantum dots: Surface localization of the photogenerated exciton. *Physical Review B* **50**, 2293-2300, doi:10.1103/PhysRevB.50.2293 (1994).

117 Oron, D. *et al.* Universal Role of Discrete Acoustic Phonons in the Low-Temperature Optical Emission of Colloidal Quantum Dots. *Physical Review Letters* **102**, 177402, doi:10.1103/PhysRevLett.102.177402 (2009).

118 Rodina, A. V. & Efros, A. L. Radiative recombination from dark excitons in nanocrystals: Activation mechanisms and polarization properties. *Physical Review B* **93**, 155427, doi:10.1103/PhysRevB.93.155427 (2016).

119 Leung, K., Pokrant, S. & Whaley, K. B. Exciton fine structure in CdSe nanoclusters. *Physical Review B* **57**, 12291-12301, doi:10.1103/PhysRevB.57.12291 (1998).